IN-91-CR
310824
P. 67

FINAL PROJECT REPORT
TO THE NATIONAL AERONAUTICS AND SPACE ADMINISTRATION

NASA Grant NAGW-1077

"Mars Tectonics and Volcanism"

for the period

1 June 1987 - 31 May 1990

Principal Investigator:
Prof. Sean C. Solomon
Department of Earth, Atmospheric,
and Planetary Sciences
Massachusetts Institute
of Technology
Cambridge, MA 02139

(NASA-CR-187351) MARS TECTONICS AND
VOLCANISM Final Technical Report, 1 June
1987 - 31 May 1990 (MIT) 67 p CSCL 03B
N91-14254
Unclas
G3/91 0310824

30 October 1990

This is the Final Technical Report on research conducted under NASA Grant NAGW-1077 entitled "Mars Tectonics and Volcanism." This grant supported the research of one Investigator (S.C. Solomon) and one Ph.D. student (P.J. McGovern) on behalf of the NASA MEVTV (Mars: Evolution of Volcanism, Tectonics, and Volatiles) Project over the three-year period 1 June 1987-31 May 1990.

The focus of the research was on three broad areas:

1) The relation between lithospheric stress in the vicinity of a growing volcano and the evolution of eruption characteristics and tectonic faulting;

2) The relation between elastic lithosphere thickness and thermal structure;

3) A synthesis of constraints on heat flow and internal dynamics on Mars.

The best means of conveying the principal findings of our research is through the publications reporting our work. On the following page is a list of publications supported under this project during the past 3 years. Included in the list are 3 papers, 2 book chapters, 7 abstracts of oral presentations, and 1 technical report.

The remainder of this report consists of two of the most recently completed papers supported by this project. The other publications listed are or have been included in other progress reports.

Publications Supported by NASA Grant NAGW-1077

McGovern, P.J., and S.C. Solomon, State of stress and eruption characteristics of martian volcanoes, in *Abstracts for the MEVTV Workshop on the Evolution of Magma Bodies on Mars*, pp. 31-32, Lunar and Planetary Institute, Houston, Tex., 1990.

McGovern, P.J., and S.C. Solomon, State of stress and eruption characteristics of martian volcanoes, in *Lunar and Planetary Science XXI*, 765-766, Lunar and Planetary Institute, Houston, Tex., 1990.

McGovern, P.J., and S.C. Solomon, State of stress, faulting, and eruption characteristics of large volcanoes on Mars, *J. Geophys. Res.*, to be submitted, 1990.

Schubert, G., S.C. Solomon, D.L. Turcotte, M.J. Drake, and N.H. Sleep, Origin and thermal evolution of Mars, in *Mars*, edited by H. Kieffer, B. Jakosky, C. Snyder, and M.S. Matthews, Univ. Arizona Press, in press, 1990.

Schubert, G., D.L. Turcotte, S.C. Solomon, and N.H. Sleep, Coupled evolution of the atmosphere and interiors of planets and satellites, in *Origin and Evolution of Planetary and Satellite Atmospheres*, edited by S.K. Atreya, J.B. Pollack, and M.S. Matthews, Univ. Arizona Press, Tucson, pp. 450-483, 1989.

Schubert, G., D.L. Turcotte, S.C. Solomon, N.H. Sleep, and M.J. Drake, Origin and thermal evolution of Mars, in *Program and Abstracts, Fourth International Conference on Mars*, pp. 50-51, Univ. Arizona, Tucson, 1989.

Solomon, S.C., Geophysics and tectonics of Mars, in *Abstracts with Programs*, *20*, A83, Geol. Soc. Amer., Boulder, Colo., 1988.

Solomon, S.C., and J.W. Head, Heterogeneities in the thickness of the elastic lithosphere of Mars: Constraints on thermal gradients, crustal thickness, and internal dynamics, in *Abstracts for the MEVTV-LPI Workshop: Early Tectonic and Volcanic Evolution of Mars*, pp. 54-56, Lunar and Planetary Institute, Houston, Tex., 1988.

Solomon, S.C., and J.W. Head, Estimating lithospheric thermal gradient on Mars from elastic lithosphere thickness: New constraints on heat flow and mantle dynamics, in *Lunar and Planetary Science XX*, 1030-1031, Lunar and Planetary Institute, Houston, Tex., 1989.

Solomon, S.C., and J.W. Head, Estimating lithospheric thermal gradient on Mars from elastic lithosphere thickness: New constraints on heat flow and mantle dynamics, in *Reports of Planetary Geology and Geophysics Program - 1988*, 203-205, 1989.

Solomon, S.C., and J.W. Head, Heterogeneities in the thickness of the elastic lithosphere of Mars: Constraints on heat flow and internal dynamics, *J. Geophys. Res.*, *95*, 11073-11083, 1990.

Zimbelman, J.R., S.C. Solomon, and V.L. Sharpton, editors, *MEVTV Workshop on Nature and Composition of Surface Units on Mars*, LPI Tech. Rep. 88-05, Lunar and Planetary Institute, Houston, 144 pp., 1988.

Zimbelman, J.R., S.C. Solomon, and V.L. Sharpton, The evolution of volcanism, tectonics, and volatiles on Mars: An overview of recent progress, *Proc. Lunar Planet. Sci. Conf. 21st*, in press, 1990.

JOURNAL OF GEOPHYSICAL RESEARCH, VOL. 95, NO. B7, PAGES 11,073–11,083, JULY 10, 1990

Heterogeneities in the Thickness of the Elastic Lithosphere of Mars: Constraints on Heat Flow and Internal Dynamics

SEAN C. SOLOMON

Department of Earth, Atmospheric, and Planetary Sciences, Massachusetts Institute of Technology, Cambridge

JAMES W. HEAD

Department of Geological Sciences, Brown University, Providence, Rhode Island

Derived values of the thickness of the effective elastic lithosphere on Mars are converted to estimates of lithospheric thermal gradients and surface heat flow by finding the thickness of the elastic-plastic plate having the same bending moment and curvature, subject to assumed strain rates and temperature-dependent flow laws for crustal and mantle material. Local thermal gradients and heat flow values so estimated were 10–14 K km^{-1} and 25–35 mW m^{-2}, respectively, at the time of formation of flexurally induced graben surrounding the Tharsis Montes and Alba Patera, while gradients and heat flow values of less than 5–6 K km^{-1} and 17–24 mW m^{-2}, respectively, characterized the lithosphere beneath the Isidis mascon and Olympus Mons at the time of emplacement of these loads. On the basis of the mean global thickness of the elastic lithosphere inferred to support the Tharsis rise and estimates of mantle heat production obtained from SNC meteorites, it is suggested that the present average global heat flux on Mars is in the range 15–25 mW m^{-2}. Approximately 3–5% of this heat flux during the Amazonian epoch has been contributed by excess conducted heat in the central regions of major volcanic provinces. Most likely, this excess heat flux has been delivered to the base of the lithosphere by mantle plumes. The fractional mantle heat transport contributed by plumes during the last 2 b.y. on Mars is therefore similar to that at present on Earth.

INTRODUCTION

The thickness of the elastic lithosphere on a planet is essentially a measure of the reciprocal of the vertical thermal gradient in the lithosphere, i.e., the depth to a temperature at which ductile behavior replaces brittle behavior at typical geological strain rates. Under flexure there is an elastic "core" of the lithosphere occupying the depth interval over which the bending stress is less than an envelope of "strength" versus depth defined by a frictional failure curve at shallow depths and a ductile flow law at greater depth [*Goetze and Evans*, 1979; *Brace and Kohlstedt*, 1980]. At the shallowest depths, lithospheric bending leads to faulting to a depth that is dependent on the load, the flexural rigidity, and the failure law. The depth of the lower limit to "elastic" behavior is governed primarily by temperature and also by strain rate, composition, and load magnitude. Estimates of elastic lithosphere thickness derived from simple models of flexure have been quantitatively related to the vertically averaged thermal gradient of the lithosphere on the Earth [e.g., *Caldwell and Turcotte*, 1979; *McNutt*, 1984; *McAdoo et al.*, 1985; *Willett et al.*, 1985; *Kusznir and Karner*, 1985] and Moon [*Solomon*, 1985], and similar concepts have been used to constrain the thickness of the elastic lithosphere on Venus [e.g., *Solomon and Head*, 1984]. In this paper we apply these concepts to Mars.

We begin with a review of estimates of the effective thickness of the Martian elastic lithosphere. We then convert these thickness values to estimates of lithospheric thermal gradients and heat flow by means of temperature-dependent strength envelopes. On the basis of the locations and geological epochs appropriate to each estimate of thermal gradient, we relate the results to global heat flux, interior thermal evolution, lithospheric reheating mechanisms, and the evolution of major volcanic provinces on Mars.

Paper number 90JB00541.
0148-0227/90/90JB-00541$05.00

ELASTIC LITHOSPHERE THICKNESS

The thickness T_e of the elastic lithosphere of Mars has been estimated from the tectonic response to individual loads [*Thurber and Toksöz*, 1978; *Comer et al.*, 1985; *Janle and Jannsen*, 1986] and from the global response to the long-wavelength load of the Tharsis rise [*Willemann and Turcotte*, 1982; *Banerdt et al.*, 1982; *Sleep and Phillips*, 1985]. A summary of these results is given in Table 1. It is important to distinguish the elastic lithosphere from the thermal or compositional lithosphere inferable from Pratt isostatic compensation models [e.g., *Sleep and Phillips*, 1979] or from the heights of volcanic constructs [*Vogt*, 1974; *Carr*, 1976]. The base of the elastic or mechanical lithosphere is governed by the temperature at which ductile strength becomes less than some threshold value at geological strain rates [*Goetze and Evans*, 1979; *Brace and Kohlstedt*, 1980].

The radial distances of graben circumferential to the major volcanoes Ascraeus Mons, Pavonis Mons, Arsia Mons, Alba Patera, and Elysium Mons (Figure 1) indicate best fitting values for flexural rigidity D of 10^{23}–10^{24} N m at the times of graben formation [*Comer et al.*, 1985]. These thicknesses are equivalent (for values of the lithospheric Young's modulus and Poisson's ratio of E = 100 GPa and ν = 0.25, respectively) to T_e in the range 20–50 km. In addition to best fitting values, *Comer et al.* [1985] obtained lower and upper bounds to T_e from formal error analysis as

PRECEDING PAGE BLANK NOT FILMED

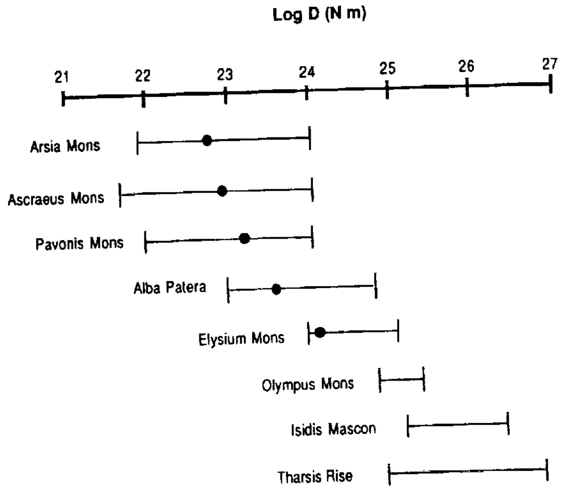

Fig. 2. Summary of estimates of the flexural rigidity of the Martian elastic lithosphere, from Table 1. The solid circles denote best fitting values [*Comer et al.*, 1985], while the bars delimit the ranges of possible values [*Willemann and Turcotte*, 1982; *Banerdt et al.*, 1982; *Comer et al.*, 1985; *Janle and Jannsen*, 1986].

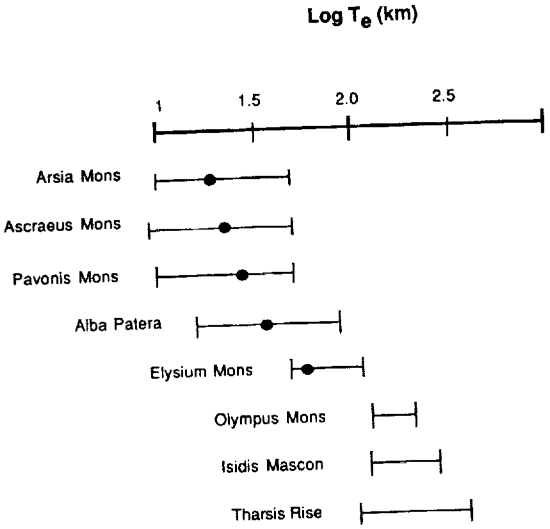

Fig. 3. Summary of estimates of the effective thickness of the elastic lithosphere of Mars, from Table 1. Symbol conventions are as in Figure 2.

sponding to at least the late Amazonian and perhaps to somewhat earlier epochs as well [*Scott and Tanaka*, 1986; *Tanaka et al.*, 1988].

A variety of models for the deep structure of the Tharsis rise have been proposed [e.g., *Sleep and Phillips*, 1979, 1985; *Banerdt et al.*, 1982; *Willemann and Turcotte*, 1982; *Finnerty et al.*, 1988]. The distribution and orientation of at least some of the tectonic features of the Tharsis province are best explained if the long-wavelength topography of the Tharsis rise was supported for a significant time by the finite strength of the global elastic lithosphere [*Willemann and Turcotte*, 1982; *Banerdt et al.*, 1982; *Sleep and Phillips*, 1985]. Quantitative models of this support that provide a reasonable fit to the geoid and to the distribution of tectonic features have an elastic lithosphere 100 to 400 km thick, corresponding to $D = 10^{25}$ to 7×10^{26} N m [*Willemann and Turcotte*, 1982; *Banerdt et al.*, 1982]. The time at which this estimate is an appropriate average for the planet depends on the evolution of the mechanism of support of long-wavelength topography [*Sleep and Phillips*, 1985] and can range from Middle Noachian (3.8 b.y. ago) to Upper Amazonian [*Tanaka*, 1986].

The best fitting values for D derived for various loads span at least 2 orders of magnitude (Figure 2), and the corresponding values for T_e span nearly a factor of 10 (Figure 3). As is apparent from Table 1 and from the discussion above, these values are not consistent with a simple progressive increase with time in the thickness of the elastic lithosphere of Mars. The largest estimates of T_e, for instance, are for the oldest (Isidis mascon) and youngest (Olympus Mons) local lithospheric loads considered. Spatial variations in elastic lithosphere thickness must therefore have been at least as important as temporal variations [*Comer et al.*, 1985]. In particular, there appears to have been a dichotomy in lithosphere thickness that spanned a significant interval of time, with comparatively thin elastic lithosphere (T_e = 20–50 km) beneath the central regions of major volcanic provinces and substantially thicker elastic lithosphere (T_e in excess of 100 km) beneath regions more distant from volcanic province centers and appropriate for the planet as a whole.

THERMAL GRADIENTS

Procedure

All of the values of T_e described above were obtained under the assumption that the elastic lithosphere of Mars behaves as a uniform elastic plate or shell. A better model for the lithosphere is an elastic-plastic plate, with the strength as a function of strain rate, plate curvature, and depth [*Goetze and Evans*, 1979; *Brace and Kohlstedt*, 1980]. To estimate the mean lithospheric thermal gradient from such an effective elastic lithosphere thickness, T_e must first be converted to the depth T_m to the rheological boundary marking the base of the mechanical lithosphere (Figure 4). This conversion is accomplished by adopting a representative strain rate and a flow law for ductile deformation of material in the lower lithosphere, constructing models of bending stress consistent with the adopted strength envelope, and finding for each model the equivalent elastic plate model having the same bending moment and curvature. This procedure has been described by *McNutt* [1984].

The temperature distribution in the mechanical lithosphere is assumed to be locally given by a surface temperature T_s of 220 K [*Kieffer et al.*, 1977; *Fanale et al.*, 1982] and a uniform vertical gradient dT/dz. We take the representative strain rate for the flexural response to each local load to be the quotient of the maximum horizontal strain given by the elastic model and the growth time of the load. On the basis of stratigraphic relations among the principal volcanic units associated with the major lithospheric loads [*Scott and Tanaka*, 1986; *Tanaka*, 1986] and the crater chronology of *Hartmann et al.* [1981], we take the load growth time to be 10^8 years. The brittle and ductile portions of the strength envelope are approximated by straight lines, so that the bending moment may be found analytically given the curvature and dT/dz [*McNutt and Menard*, 1982; M. K. McNutt, personal communication, 1988]. The brittle portion of the strength envelope is taken from the low-pressure friction law of *Byerlee* [1978], with a lithostatic pressure gradient appropriate to the Martian crust (11 MPa km^{-1}) under the assumption of negligible pore pressure. If the mechanical lithoeffective Young's modulus is not well known for Mars, to first order the resulting relative uncertainty in T_e is only one third that in E. In general, of course, curvature is not a constant but varies along a flexural profile; it may be argued [*McNutt*, 1984], however, that the estimates of D and T_e in Table 1 are dominated by the portions of the profiles at which bending stress, and thus curvature, are near their maximum values, so we assume such maximum values in using Figures 5 and 6.

The effective surface temperature T_s has an uncertainty of perhaps 20–30 K. The mean microwave brightness temperature of Mars is about 200 K [*Morrison et al.*, 1969]. Climate models for Mars predict that the present seasonally averaged surface temperature should vary with latitude and should be 200–230 K at the latitudes (approximately 40°N to 10°S) of the features listed in Table 1 [*Kieffer et al.*, 1977; *Fanale et al.*, 1982]. Such models do not generally include variations in topography, which likely would add a superposed variation in surface temperature of perhaps 10–20 K [*Seiff and Kirk*, 1977] for the range in regional elevations of prominent lithospheric loads. An additional uncertainty is contributed by poorly constrained differences between the present climate of Mars and that at the time of load-induced graben formation. A final factor is the possible presence of a low-conductivity regolith layer, which can be accommodated in the simple model adopted here by use of a small increase in T_s [*McNutt and Menard*, 1982]. A 20–30 K uncertainty in T_s contributes only a 3–7% uncertainty to estimates of lithospheric thermal gradient and heat flow.

The assumption of a linear thermal gradient can also be questioned. In effect, for a given strain rate and flow law the quantity T_m essentially gives the depth to a particular temperature, and any temperature distribution that passes through that temperature-depth point and the surface temperature T_s (and that does not exceed the limiting temperature at depths less than T_m) should be regarded as possible. Effects such as upward concentration of crustal heat-producing elements and a thermal conductivity that increases with depth will tend to give a temperature distribution that is concave downward, so that near-surface gradients will be higher than those indicated in Figures 5 and 6. Further, there is also at least an order or magnitude uncertainty in the growth time of the lithospheric loads utilized to estimate T_e and thus in the effective flexural strain rate. A factor of 10 uncertainty in growth time, however, contributes only a 4% uncertainty to the derived values of T_m or dT/dz for either of the adopted flow laws.

A source of uncertainty is the abundance of water in the Martian interior. In the upper crust a significant pore pressure can lower the frictional strength [*Brace and Kohlstedt*, 1980], which would result in modest increases in T_m (or decreases in dT/dz) for given values of elastic thickness and curvature. Whether water is present in the lower crust and upper mantle of Mars is an issue for the estimation of ductile strength, since the presence of water can significantly affect creep rates in rock [e.g., *Ashby and Verrall*, 1977]. The adopted olivine flow law, although derived from laboratory measurements, has been reasonably well validated for the terrestrial oceanic mantle and geological strains rates, by means of both flexural estimates of mechanical lithosphere thickness [*McNutt and Menard*, 1982; *McNutt*, 1984] and centroid depths of intraplate earthquakes [*Bergman and Solomon*, 1984], although *McNutt and Menard* [1982] have suggested that the activation energy for creep in the mantle may be slightly less than that obtained from laboratory measurements on dry olivine. For Mars we note that significant water in the mantle and an activation energy less than that assumed here [*Goetze*, 1978] would both result in lower estimates of thermal gradient than shown in Figure 5; we comment on this point further below.

The flow law for crustal material is probably less well constrained in general than that for the mantle. To explore at least partially the effect of this uncertainty, we also considered the flow law of anorthosite reported by *Shelton* [1981]. Values of T_m and dT/dz differ by about 5–15% from those obtained with the diabase flow law of *Caristan* [1982] for strain rates in the range 10^{-16} to 10^{-19} s^{-1}. The straight-line approximation to the ductile portion of the strength envelope, while a reasonable simplification for the olivine flow law [*McNutt and Menard*, 1982], with flow laws for crustal material leads to an underestimate of ductile strength in the lowermost mechanical lithosphere and thus a slight increase in estimated T_m, for an assumed constant strain rate.

A considerable uncertainty in the application of relations such as those depicted in Figures 5 and 6 arises from our poor knowledge of the thickness of the Martian crust. Long-wavelength topography and gravity, if intepreted in terms of a crust of uniform density and variable thickness, indicate a mean crustal thickness of at least 30 km [*Bills and Ferrari*, 1978], which corresponds to zero crustal thickness beneath the Hellas basin. Models of the Viking line of sight (LOS) Doppler radio tracking residuals over the Hellas basin and the 370-km-diameter crater Antoniadi are consistent with essentially local Airy compensation if the crust beneath these impact features is 120–130 km thick [*Sjogren and Wimberly*, 1981; *Sjogren and Ritke*, 1982]. From the models of *Bills and Ferrari* [1978] a 130-km-thick crust beneath the Hellas basin [*Sjogren and Wimberly*, 1981] corresponds to a globally averaged crustal thickness of about 150 km. LOS tracking data over Elysium Planitia and Olympus Mons can be fit with varying degrees of Airy isostatic compensation and crustal thicknesses of 30–150 km [*Janle and Ropers*, 1983; *Janle and Jannsen*, 1986]. Available gravity data are thus permissive of a mean crustal thickness anywhere in the range 30–150 km, an interval consistent with, but not substantially narrowed by, the predictions of differentiation models of an early Martian magma ocean [*Warren*, 1988]. Whatever the mean crustal thickness, local variations of ±30 km or more are also likely [*Phillips et al.*, 1973; *Bills and Ferrari*, 1978].

Given these uncertainties, our approach is to assume that the large values of elastic lithosphere thickness ($T_e > 100$ km) determined from the local response to the Isidis mascon and Olympus Mons and from the global response to the Tharsis rise exceed the thickness of the Martian crust, while the values of 20–30 km obtained for T_e beneath the Tharsis Montes and Alba Patera (Table 1) are less than or comparable to the thickness of the crust. This assumption is consistent with known constraints on the crustal thickness and, because of the lesser creep resistance of crustal material, results in minimizing the spread in inferred thermal gradients.

Finally, it should be noted that the estimation of mechanical lithosphere thickness and thermal gradient is made under the assumption that flexural stresses dominated the local lithospheric stress field at the time of load-induced

[1985] and *Laul et al.* [1986] have inferred that the mantle plus crust of the SNC parent body has a U abundance of 16 ppb, a Th/U ratio of 3.5, and a K/U ratio of 2×10^4. For an inferred mass fraction of 22% for an Fe-FeS core [*Dreibus and Wänke*, 1985; *Laul et al.*, 1986] the U abundance expressed as a fraction of the whole planet is 12.5 pbb. The present heat production for such bulk abundances is equivalent, under steady state, to a mean heat flow of 14 mW m^{-2}. *Treiman et al.* [1986] obtain element-element correlations similar to those of *Dreibus and Wänke* [1985] and *Laul et al.* [1986], with slightly smaller Th/U and K/U ratios (3.0 and 1×10^4, respectively), which for the same bulk U abundance would give a heat production about 20% lower.

These values of heat flow may be compared with the thermal gradients in Table 1 and corresponding estimates of thermal conductivity. For Tharsis Montes and Alba Patera, T_m is less than the crustal thickness, so we adopt a thermal conductivity appropriate for crustal material, 2.5 W m^{-1} K^{-1} [*Clark*, 1966]. Lithospheric thermal gradients of 10–14 K km^{-1} (Table 1) correspond to heat flow values of 25–35 mW m^{-2}. For the mechanical lithosphere supporting Olympus Mons, the Isidis mascon, and the Tharsis rise, most of the lithosphere probably consists of mantle material, so we adopt the thermal conductivity given by *Schatz and Simmons* [1972] for olivine ($Fo_{86}Fa_{14}$) at 560–930 K: 4 W m^{-1} K^{-1}. Mean lithospheric gradients less than 5–6 K km^{-1} (Table 1) then correspond to heat flow values less than 20–24 mW m^{-2}. These last estimates of heat flow, and the associated temperature distributions depicted in Figure 7, should be reduced to be consistent with the likely contrast in thermal conductivity and gradients across the crust-mantle boundary, but in order to do so a crustal thickness must be assumed. For a crust 30–50 km thick and the above values of crustal and mantle thermal conductivity the upper bound on heat flow consistent with mean lithospheric gradients less than 5–6 K km^{-1} is 17–21 mW m^{-2}. A global elastic lithosphere at least 100 km thick, indicated by flexural models for the support of the Tharsis rise [*Willemann and Turcotte*, 1982; *Banerdt et al.*, 1982], implies lithospheric gradients of 7 K km^{-1} or less. The corresponding upper bound on heat flow is 23–25 mW m^{-2} for a mean crustal thickness of 30–50 km.

Thermal gradients at or near the upper end of the range allowed for Olympus Mons, Isidis, and the globally averaged response to Tharsis thus give heat flow values similar to or slightly larger than that expected from U, Th, and K abundances in SNC meteorites under the steady state assumption. Such upper bounds on thermal gradients are also consistent with a modest contribution to heat flow from secular cooling of the mantle [e.g., *Schubert et al.*, 1979]. Most published thermal history models for Mars, in contrast, predict a heat flow larger than that permitted by these upper bounds, a result attributable to an overestimation of heat production in the interior. We suggest that the global heat flux on Mars during the Amazonian epoch (approximately the last 2 b.y. [*Tanaka*, 1986]) has been in the range 15–25 mW m^{-2}. This inference is in agreement both with the thermal gradients implied by the thick elastic lithosphere beneath Olympus Mons and globally supporting the Tharsis rise and with the bulk abundances of heat-producing elements in Mars inferred from SNC meteorites. Regional heat flow in the centers of major volcanic provinces of Mars during the Amazonian epoch reached highs of 35 mW m^{-2} or more, as much as twice the typical global value.

A final point of comparison with the thermal gradients in Table 1 and Figure 7 is provided by estimates of the thickness of the thermal lithosphere made from the heights of volcanic constructs and a hydrostatic model for magmatic overpressure [*Vogt*, 1974; *Carr*, 1976; *Blasius and Cutts*, 1976]. Such estimates are quite approximate, given uncertainties contributed by differential compressibility between magma and surrounding rock, viscous head loss in the magma conduit, and additional overpressure contributed by magmatic volatiles, as well as by the probably oversimplified notion of a continuous magma column extending from a basal magma chamber to the volcano summit. We consider such models here merely as tests of consistency. For instance, the thermal gradient shown in Figure 7 for Olympus Mons, if continued downward, reaches a temperature of 1670 K, the 2.3-GPa solidus temperature of a model Martian mantle [*Bertka and Holloway*, 1988], at a depth of 285 km. Inasmuch as the volcano stands about 24 km higher than the surrounding terrain [*Wu et al.*, 1984], this relief is consistent with the thermal gradient shown and with the hydrostatic head model if the average effective density contrast between magma and the surrounding rock column is about 8%, a quite reasonable value. The lesser relief (14–18 km) of the Tharsis Montes volcanoes [*Blasius and Cutts*, 1976] is consistent with the higher thermal gradients indicated for the lithosphere beneath these features (Table 1 and Figure 7), but quantitative agreement with the magma hydrostatic model would require consideration of distinct densities and thermal conductivities for the crust and mantle, lateral variations in crustal thickness [*Blasius and Cutts*, 1976], and the possible contribution of convective flow to heat transport in the lower lithosphere beneath the central Tharsis region.

Evolution of the Tharsis Province

As noted above, considerable attention has been devoted to the deep structure and evolution of the Tharsis volcanic and tectonic province. While the long-wavelength gravity and topography of the region are not consistent with complete local isostatic compensation by a single mechanism such as crustal thickness variations [*Phillips and Saunders*, 1975], complete local compensation is possible if a combination of Airy (crustal thickness variations) and Pratt (lateral density variations) mechanisms act in concert, but only if the crust is relatively thin (or is pervasively intruded by high-density plutonic material) beneath the Tharsis rise and substantial density anomalies persist to at least 300–400 km depth [*Sleep and Phillips*, 1979, 1985; *Finnerty et al.*, 1988]. Alternatively, the gravity and topography are consistent with the hypothesis that a portion of the high topography of Tharsis is supported by membrane stresses in the Martian elastic lithosphere [*Willemann and Turcotte*, 1982; *Banerdt et al.*, 1982; *Sleep and Phillips*, 1985].

These compensation models have been used to calculate lithospheric stresses for comparison with the observed distribution of tectonic features. The isostatic models for Tharsis predict stresses in approximate agreement with the distribution and orientation of extensional fractures in the central Tharsis region and of compressive wrinkle ridges oriented approximately circumferential to the center of tectonic activity, while the models involving lithospheric modest areas immediately surrounding localized lithospheric loads. The areas within major volcanic provinces for which the enhanced thermal gradients of Table 1 and Figure 7 are appropriate, unfortunately, are poorly constrained. Nonetheless, an approximate measure of the lateral extent of enhanced lithospheric heating is the area of regionally elevated topography arising either from remaining excess heat or, more likely, from a crust permanently thickened by the addition of volcanic and intrusive material. We assume that the areas of excess thermal gradient in the central Tharsis, central Elysium, and Alba Patera regions are 3×10^6 km^2, 0.9×10^6 km^2, and 0.8×10^6 km^2, respectively. These areas correspond to the regions encompassed by the 7.5-km, 1-km, and 5-km elevation contours in the respective provinces [*U.S. Geological Survey*, 1989]. The 7.5-km contour in the Tharsis region encloses the area of the Tharsis Montes, but not Olympus Mons, for which a lithosphere thickness and thermal gradient nearer to the global average values are indicated (Table 1). For excess thermal gradients of about 10 K km^{-1} in central Tharsis and 5 K km^{-1} in the other two volcanic provinces (Table 1) and a crustal thermal conductivity of 2.5 W m^{-1} K^{-1} the heat delivered by these excess gradients is at a rate of 1×10^{11} W, with 80% of the contribution to this figure coming from the Tharsis region. This figure is 3–5% of the estimated present global heat loss, 2–4 $\times 10^{12}$ W for the probable range of average heat flux values given above. By way of comparison the fraction of mantle heat flux delivered by plumes at present on Earth has also been estimated to be about 5% [*Davies*, 1988; *Sleep*, 1990]. The heat delivered by plumes on Mars must be supplied by cooling of the Martian core. In the thermal history models of *Stevenson et al.* [1983] the Martian core delivers heat to the mantle at a rate of 2×10^{11} W during the Amazonian, sufficient to supply the estimated heat transported by plumes beneath major volcanic provinces.

We may compare these figures to the fractional heat flow delivered by volcanism and associated igneous intrusions. Estimates of the surface area of volcanic material at each major stratigraphic stage, including corrections for later burial, have been given by *Greeley* [1987] and *Tanaka et al.* [1988]. Both find 2×10^8 km^2 of volcanic material, though the two analyses differ in detail, particularly in the relative strength of a "peak" in the flux curve at early Hesperian times (corresponding to the formation of the Martian ridged plains) about 3–3.5 b.y. ago [*Tanaka*, 1986]. *Greeley* [1987] has suggested that the volume of volcanic material may be estimated by multiplying the area by an average thickness of about 1 km. A volume V of 2×10^8 km^3 may be converted to equivalent heat Q by means of the relation $Q = \rho(C_p\Delta T + \Delta H)V$, where ρ is the density of volcanic material, C_p is the specific heat, ΔT is the difference between eruption and ambient temperatures, and ΔH is the heat of fusion. We take $\rho = 3$ Mg m^{-3}, $C_p = 1.2$ kJ kg^{-1} K^{-1}, and $\Delta H = 0.4$ MJ kg^{-1}, and we adopt $\Delta T = 1450$ K [*Bertka and Holloway*, 1988]. Averaged over 3.8 b.y., 2×10^8 km^3 of volcanic material delivers only 10^{10} W, or less than 1%, of the estimated present global heat loss of 2–4 $\times 10^{12}$ W. Accompanying any volcanic eruption, of course, is usually a significant intrusion of magma that cools and solidifies at depth. The ratio of intruded to extruded volumes is as great as 10:1 in terrestrial eruptions [*Crisp*, 1984]. The combined volumes of volcanic and intrusive material on Mars, for this ratio, would have delivered heat at an average rate of 3–6% of the total global heat loss. Note that the intrusive component of igneous activity may find expression in the inferred conductive gradient, depending on the depth of intrusion, but the volcanic component of activity will not.

The volcanic flux has decreased sharply with time over Martian history [*Greeley*, 1987; *Tanaka et al.*, 1988], so it is worth making a similar calculation both for the periods of high volcanic output as well as for the Amazonian epoch corresponding to most of the estimates of lithosphere thickness and thermal gradient given in Table 1 and Figure 7. For both the mid-Noachian and early Hesperian epochs, volcanism resurfaced large areas in widespread regions over the planet. With the areas of volcanic material given by *Tanaka et al.* [1988] for these periods, the 1-km thickness estimate of *Greeley* [1987], and the time intervals given by *Tanaka* [1986], the heat delivered by volcanism was at rates of 2×10^{11} and 3×10^{10} W, respectively. For a 10:1 ratio of intrusive to erupted material the heat flux delivered by magmatism during the mid-Noachian may have been as much as one third of the global heat flux, with the precise ratio depending on mantle heat production, global thermal history, and the uncertain duration of the epoch. In contrast, the heat delivered by volcanism and plutonism estimated by this same procedure for the Amazonian contributed on average no more than 4×10^{10} W, a figure equal to about 40% of the excess conducted heat at major volcanic centers, estimated above, and only 1–2% of the global heat loss.

CONCLUSIONS

Estimates of the thickness of the effective elastic lithosphere of Mars appropriate to a variety of locations and times have been converted to estimates of lithospheric thermal gradient and surface heat flow by means of strength envelope considerations. Local thermal gradients and heat flow values were 10–14 K km^{-1} and 25–35 mW m^{-2} at the time of formation of load-induced graben surrounding the Tharsis Montes and Alba Patera, while gradients and heat flow values of less than 5–6 K km^{-1} and 17–24 mW m^{-2} characterized the lithosphere beneath the Isidis mascon and Olympus Mons at the time of emplacement of these loads. On the basis of the thickness of the global elastic lithosphere required to support the Tharsis rise, inferred on thermal grounds to characterize a late, rather than an early, stage in the evolution of the Tharsis province [cf. *Sleep and Phillips*, 1985], as well as heat production estimates obtained from SNC meteorites, we suggest that the present global heat flux on Mars is in the range 15–25 mW m^{-2}. Approximately 3–5% of this heat flux during the Amazonian epoch has been contributed by excess conducted heat in the central regions of major volcanic provinces, a figure at least a factor of 3 greater than the heat transported solely by volcanism and shallow igneous intrusions. This excess heat flux is plausibly attributed to the action of mantle plumes on the base of the lithosphere beneath volcanic province centers. The fractional mantle heat transport contributed by plumes during the last 2 b.y. on Mars is therefore comparable to the present situation on Earth.

Acknowledgments. We are grateful to Marcia McNutt for providing the computer program with which we generated Figures 5 and 6, and we thank Linda Meinke and Mary Shearer for assistance with figure preparation. We appreciate helpful comments on an earlier

Schultz, P. H., and H. Glicken, Impact crater and basin control of igneous processes on Mars, *J. Geophys. Res.*, *84*, 8033–8047, 1979.

Sclater, J. G., C. Jaupart, and D. Galson, The heat flow through oceanic and continental crust and the heat loss of the Earth, *Rev. Geophys.*, *18*, 269–312, 1980.

Scott, D. H., and M. H. Carr, Geologic map of Mars, *Map I-1083*, U.S. Geol. Surv., Reston, Va., 1978.

Scott, D. H., and K. L. Tanaka, Geologic map of the western equatorial region of Mars, *Map I-1802-A*, U.S. Geol. Surv., Reston, Va., 1986.

Seiff, A., and D. B. Kirk, Structure of the atmosphere of Mars in summer at mid-latitudes, *J. Geophys. Res.*, *82*, 4364–4378, 1977.

Shelton, G., Experimental deformation of single phase and polyphase crustal rocks at high pressures and temperatures, Ph.D. thesis, 146 pp., Brown Univ., Providence, R. I., 1981.

Sjogren, W. L., and S. J. Ritke, Mars: Gravity data analysis of the crater Antoniadi, *Geophys. Res. Lett.*, *9*, 739–742, 1982.

Sjogren, W. L., and R. N. Wimberly, Mars: Hellas Planitia gravity analysis, *Icarus*, *45*, 331–338, 1981.

Sleep, N. H., Hotspots and mantle plumes: Some phenomenology, *J. Geophys. Res.*, *95*, 6715–6736, 1990.

Sleep, N. H., and R. J. Phillips, An isostatic model for the Tharsis province, Mars, *Geophys. Res. Lett.*, *6*, 803–806, 1979.

Sleep, N. H., and R. J. Phillips, Gravity and lithospheric stress on the terrestrial planets with reference to the Tharsis region of Mars, *J. Geophys. Res.*, *90*, 4469–4489, 1985.

Solomon, S. C., The elastic lithosphere: Some relationships among flexure, depth of faulting, lithospheric thickness, and thermal gradient (abstract), *Lunar Planet. Sci.*, *16*, 799–800, 1985.

Solomon, S. C., and J. Chaiken, Thermal expansion and thermal stress in the Moon and terrestrial planets: Clues to early thermal history, *Proc. Lunar Sci. Conf.*, *7th*, 3229–3243, 1976.

Solomon, S. C., and J. W. Head, Lunar mascon basins: Lava filling, tectonics, and evolution of the lithosphere, *Rev. Geophys.*, *18*, 107–141, 1980.

Solomon, S. C., and J. W. Head, Evolution of the Tharsis province of Mars: The importance of heterogeneous lithospheric thickness and volcanic construction, *J. Geophys. Res.*, *87*, 9755–9774, 1982.

Solomon, S. C., and J. W. Head, Venus banded terrain: Tectonic models for band formation and their relationship to lithospheric thermal structure, *J. Geophys. Res.*, *89*, 6885–6897, 1984.

Stevenson, D. J., T. Spohn, and G. Schubert, Magnetism and thermal evolution of the terrestrial planets, *Icarus*, *54*, 466–489, 1983.

Tanaka, K. L., The stratigraphy of Mars, *Proc. Lunar Planet. Sci. Conf. 17th*, *Part* 1, *J. Geophys. Res.*, *91*, Suppl., E139–E158, 1986.

Tanaka, K. L., N. K. Isbell, D. H. Scott, R. Greeley, and J. E. Guest, The resurfacing history of Mars: A synthesis of digitized, Viking-based geology, *Proc. Lunar Planet. Sci. Conf.*, *18th*, 665–678, 1988.

Thurber, C. H., and M. N. Toksöz, Martian lithospheric thickness from elastic flexure theory, *Geophys. Res. Lett.*, *5*, 977–980, 1978.

Toksöz, M. N., and A. T. Hsui, Thermal history and evolution of Mars, *Icarus*, *34*, 537–547, 1978.

Toksöz, M. N., A. T. Hsui, and D. H. Johnston, Thermal evolutions of the terrestrial planets, *Moon Planets*, *18*, 281–320, 1978.

Treiman, A. H., M. J. Drake, M.-J. Janssens, R. Wolf, and M. Ebihara, Core formation in the Earth and shergottite parent body (SPB): Chemical evidence from basalts, *Geochim. Cosmochim. Acta*, *50*, 1071–1091, 1986.

Turcotte, D. L., F. A. Cooke, and R. J. Willemann, Parameterized convection within the Moon and the terrestrial planets, *Proc. Lunar Planet. Sci. Conf.*, *10th*, 2375–2392, 1979.

U.S. Geological Survey, Topographic maps of the western, eastern equatorial and polar regions of Mars, *Map I-2030*, Reston, Va., 1989.

Vogt, P. R., Volcano height and plate thickness, *Earth Planet. Sci. Lett.*, *23*, 337–348, 1974.

Warren, P. H., Primordial global differentiation, Mars-style (abstract), in *Abstracts for the MEVTV-LPI Workshop: Early Tectonic and Volcanic Evolution of Mars*, pp. 60–62, Lunar and Planetary Institute, Houston, Tex., 1988.

Watters, T. R., and T. A. Maxwell, Crosscutting relations and relative ages of ridges and faults in the Tharsis region of Mars, *Icarus*, *56*, 278–298, 1983.

Watters, T. R., and T. A. Maxwell, Orientation, relative age, and extent of the Tharsis Plateau ridge system, *J. Geophys. Res.*, *91*, 8113–8125, 1986.

Wetherill, G. W., Occurrence of giant impacts during the growth of the terrestrial planets, *Science*, *228*, 877–879, 1985.

Willemann, R. J., and D. L. Turcotte, The role of lithospheric stress in the support of the Tharsis rise, *J. Geophys. Res.*, *87*, 9793–9801, 1982.

Willett, S. D., D. S. Chapman, and H. J. Neugebauer, A thermomechanical model of continental lithosphere, *Nature*, *314*, 520–523, 1985.

Wu, S. S. C., P. A. Garcia, R. Jordan, F. J. Schafer, and B. A. Skiff, Topography of the shield volcano, Olympus Mons on Mars, *Nature*, *309*, 432–435, 1984.

Zhang, J., and T. Wong, Lithospheric flexure and deformation-induced gravity changes: Effect of elastic compressibility and gravitation on a multilayered, thick plate model, *Geophys. J.*, *92*, 73–88, 1988.

J. W. Head, Department of Geological Sciences, Brown University, Providence, RI 02912.

S. C. Solomon, Department of Earth, Atmospheric, and Planetary Sciences, Room 54-522, Massachusetts Institute of Technology, Cambridge, MA 02139.

(Received February 22, 1989;
revised November 9, 1989;
accepted November 14, 1989.)

STATE OF STRESS, FAULTING, AND ERUPTION CHARACTERISTICS OF LARGE VOLCANOES ON MARS

Patrick J. McGovern and Sean C. Solomon

Department of Earth, Atmospheric, and Planetary Sciences
Massachusetts Institute of Technology
Cambridge, MA 02139

To be submitted to the *Journal of Geophysical Research*

ABSTRACT

The formation of a large volcano loads the underlying lithospheric plate and can lead to lithospheric flexure and faulting. In turn, lithospheric stresses affect the stress field beneath and within the volcanic edifice and can influence magma transport. Modeling the interaction of these processes is crucial to an understanding of the history of eruption characteristics and tectonic deformation of large volcanoes. We develop preliminary models of time-dependent stress and deformation for the Tharsis volcanoes on Mars. A finite element code is used that simulates viscoelastic flow in the mantle and plate buoyancy forces. We show the manner in which time-dependent stresses induced by lithospheric plate flexure beneath the volcanic load may affect eruption histories, and we suggest that the stress field may be relatable to tectonic features on and surrounding Martian volcanoes. After an initial load, flexurally-induced stresses grow with time and the principal stress directions in the volcano rotate as flexure proceeds. Magma is expected to propagate perpendicular to the least compressive stress axis. As a result of flexure, this axis rotates from a horizontal orientation to a nearly vertical one; thus magma propagation paths will tend to rotate from vertical to horizontal orientations. We suggest that at the later stages of flexure, this effect would tend to favor eruption sites on to the flanks of the volcano rather than the summit. Such a scenario is consistent with the photogeologically determined evolution of the Tharsis Montes. During flexure there are three regions where stresses become sufficiently large to cause failure by faulting (according to the Mohr-Coulomb criterion): at the surface of the plate just outward of the edge of the volcano, on the volcano's flanks, and inside the plate beneath the center of the volcano. Normal faulting is the dominant mode of failure predicted for the first region, consistent with circumferential graben observed around the Tharsis Montes and with the scarp at the base of Olympus Mons, interpreted as a large-offset, listric normal fault. Failure in the second region is predicted to consist of thrust faulting, oriented mostly circumferentially on the upper flanks with a narrow annulus of radially oriented thrust faulting about midway downslope. Concentric terraces, interpreted by some workers as thrust faults, on the upper flanks of Olympus Mons may correspond to the predicted circumferential thrust features. Normal faulting, mostly

radially oriented, is predicted for the mid-plate zone of failure beneath the volcano. Under the premise that failure in this zone may be strongly influenced by pre-existing weak zones or regional stresses, this feature may have a surface expression in the rifting and the bilateral symmetry of the Tharsis Montes.

INTRODUCTION

The major Tharsis volcanoes of Mars (Olympus Mons and the three Tharsis Montes: Arsia Mons, Pavonis Mons and Ascraeus Mons) are among the largest known volcanic structures in the solar system. An understanding of the formation and evolution of these structures can provide important constraints on the processes that built and maintained the Tharsis rise. In addition, the Tharsis volcanoes may be analogues to large hot-spot volcanoes on Earth, such as Kilauea on Hawaii. For instance, Kilauea and Olympus Mons have very similar ratios of volcano height to diameter and of basal scarp height to volcano height (*Borgia et al.*, 1990). Thus studies of the evolution of large Martian volcanoes may yield insight into terrestrial volcanic processes as well. In this paper we utilize finite element models to evaluate the evolution in internal stress and deformation within and surrounding the Tharsis volcanoes, and we discuss how the time-dependent stress field may be relatable to the eruption characteristics of the volcanoes and to the formation of associated tectonic features.

To date the investigation of the evolution of stresses in large volcanoes has taken two paths: models of edifice stresses alone (usually finite element models with rigid bottom boundary conditions), and investigations of flexural stresses in the lithospheric plate supporting the volcano. As examples of the first category of study, *Chevallier and Verwoerd* (1988) used an axisymmetric planar finite element code to investigate the effect of magma chamber and external pressures on stress and eruption histories of hot spot volcanoes, *Dieterich* (1988) modeled stress in volcano rift zones by means of a two-dimensional triangular grid of elements, and *Ryan* (1988) employed a horizontal planar finite element model of the flank of Kilauea to determine displacements and stresses due to dike emplacement. In an example of the second class of study, *Thurber and Gripp* (1988) applied a flexure model to constrain the tectonics of volcano flank motions. *ten Brink and Brocher* (1987) proposed a link between flexural stresses in the lithosphere and eruption history; in their scenario the orientation of flexural stresses beneath a given point on the volcanic chain changes with time as the volcanic load is emplaced and then eroded. Given that magma seeks to propagate along paths perpendicular to the least compressive stress direction, magma ascent can be blocked when both principal horizontal stress deviators are compressional. Thus eruption history depends on location along the volcanic chain or on time since volcano formation.

Recently studies have been carried out on edifice stresses of large Martian volcanoes. *Zuber and Mouginis-Mark* (1990) treated the evolution of the surface of Olympus Mons, using a finite element model to calculate stresses in the summit caldera region caused by different magma chamber locations and geometries and to compare those stresses with patterns of faulting. *Thomas et al.* (1990) investigated the tectonics of the flanks of Martian volcanoes by means of an incompressible finite-element model. Volcano self-loading and magma chamber effects were included, but lithospheric flexure was not. Thomas and coworkers found that stresses on the flanks of a large volcano are sufficient to cause circumferentially oriented thrust faulting, and they suggested that such thrusting produced the concentric terraces observable high on the flanks of Olympus Mons.

In this paper we study the stress field within a volcano and the lithosphere upon which it rests as a unified system. With such a model formulation we can account explicitly for the interaction between edifice stresses (e.g., due to volcano self-loading) and flexural stresses (a result of the load induced by the volcano on the lithosphere). We include viscoelastic deformation in the asthenosphere, so the problem is intrinsically time-dependent. The calculated displacements yield the subsidence history of the volcano. The orientations of principal stresses and their change with time provide important constraints on possible magma emplacement paths and eruption histories. With the computed stress fields, a failure criterion can be used to predict locations and modes of faulting within and near the volcano. After a short discussion of important geological and geophysical characteristics of the Tharsis volcanoes, we briefly describe the finite element procedure and the modelling assumptions. The results of the numerical computations are next presented, and their potential implications for the evolution of eruption characteristics and for the formation of tectonic features are compared with known constraints on the evolution of the Tharsis volcanoes.

CHARACTERISTICS OF MAJOR THARSIS VOLCANOES

The four major Tharsis volcanoes are the largest of the martian shield volcanoes (e.g., *Greeley and Spudis*, 1981). Each construct is composed of many overlapping flows and flow units erupted over a period of activity as much as 2-3 b.y. in duration (*Tanaka*, 1986). The approximate heights and basal diameters are given in Table 1.

The largest of the major Tharsis volcanoes is Olympus Mons (Figure 1). The principal tectonic features associated with Olympus Mons are (1) the summit caldera complex, consisting of a series of circular depressions with complex patterns of faulting, (2) the basal scarp, a nearly vertical cliff surrounding the volcano at a radius of about 300 km. Of less certain origin are (3) the aureole deposits, which occupy a vast region dominantly to the northwest of the main shield (downslope from the Tharsis rise), and (4) concentric terraces seen on the upper slopes of the volcano. The summit caldera is likely the result of a collapse following withdrawal of magma from a high-level magma chamber (*Mouginis-Mark*, 1981; *Zuber and Mouginis-Mark*, 1990). The basal scarp has been variously interpreted as a thrust fault (*Morris*, 1981), a listric normal fault (*Francis and Wadge*, 1983), and a fault-propagation fold over a subsurface thrust fault (*Borgia et al.*, 1990). The aureole deposits are generally held to be disrupted landslide material derived from the slopes of the volcano (*Harris*, 1977; *Lopes et al.*, 1980; *Francis and Wadge*, 1983). As noted earlier *Thomas et al.* (1990) have interpreted the concentric terraces to be thrust faults.

Tectonic features observed on and around the Tharsis Montes volcanoes differ somewhat from those of Olympus Mons. Noteworthy are the circumferential graben which occur on the lower volcano slopes and the surrounding plains (Figures 2-5). The Tharsis Montes volcanoes exhibit a qualitative bilateral symmetry about a NE-SW-trending axis coinciding approximately with the line connecting their centers. From photogeological study of Viking Orbiter images, *Crumpler and Aubele* (1978) proposed the following evolutionary sequence for the Tharsis Montes: (1) construction of the main shield, (2) outbreak of parasitic eruption centers on the volcano flanks along the NE-SW-trending axis, (3) subsidence of the summit and formation of concentric fractures and graben, and (4) formation of a bisecting rift along the NE-SW-trending axis, with rift eruptions leading to flooding of the summit depression and inundation of the rifted flanks. This evolution is most developed on Arsia Mons; Pavonis Mons has reached stage (3), and Ascraeus Mons stage (2).

Comer et al. (1985) inferred the thickness of the elastic lithosphere beneath the Tharsis Montes volcanoes from the radial distances of their circumferential graben (see Figures 3-5). Preferred values of elastic lithosphere thickness are around 20 km. Concentric graben are not found around Olympus Mons, which led Comer and others to conclude that the elastic lithosphere thickness under Olympus Mons must be much greater (> 150 km) than beneath the Tharsis Montes. Of course, the actual lithosphere does not behave perfectly elastically; rather its strength is limited by frictional failure at shallow depth and by ductile flow at greater depth. From strength envelope considerations for crustal and mantle material (*McNutt*, 1984), values for elastic plate thickness were converted into estimates of mechanical plate thickness by *Solomon and Head* (1990).

METHOD

We use the finite element program TECTON (*Melosh and Rafesky*, 1980, 1983) to model stresses and displacements in a large volcano and in the crust and mantle beneath and around the volcano. TECTON's capability for adopting a viscoelastic rheology allows us to model time-dependent plate flexure. The program first calculates the elastic (i.e., "instantaneous") response to the load. The stresses and displacements arising from load-induced viscoelastic flow in the mantle are then calculated for a specified number of time steps. The Maxwell time (τ_M) of the mantle, defined as the ratio of viscosity η to shear modulus μ, is used as a convenient reference time scale. For all computations here, timesteps were implemented in three groups. The first group had timesteps of duration about equal to τ_M and were run up to $10\,\tau_M$; the second group had steps of $10\,\tau_M$ run up to $100\,\tau_M$, and the third group used steps of $100\,\tau_M$ ending at $1000\,\tau_M$. Results shown here were obtained at approximately 10, 100, and 1000 Maxwell times.

We assume that the problem is axisymmetric, with cylindrical coordinates r, θ, and z. Out of plane shear stresses $\sigma_{r\theta}$ and $\sigma_{\theta z}$ are then zero. We solve for r and z displacements and stresses σ_{rr}, $\sigma_{\theta\theta}$, σ_{zz}, and σ_{rz}. In axial symmetry, two principal stresses are confined to the rz plane; thus $\sigma_{\theta\theta}$ must also be a principal stress. An example of the finite element grid used for this study is shown in Figure 6. The displacement boundary conditions are that nodes on the side walls ($r = 0$ and $r = r_{\max}$) are fixed in r but free to move in z, and that nodes on the bottom boundary ($z = -940$ km in the example shown) are fixed in z but free to move in r. The lower corners of the box are fixed in both directions. The volcano in the example has a radius of 200 km and is 20 km in height, the approximate present dimensions of Ascraeus Mons. In Figure 6 the volcano is the triangular region in the upper left-hand corner. The volcano rests on top of an elastic lithospheric plate of thickness T_e. All elements in the volcanic edifice and the plate have a high viscosity appropriate to the lithosphere. These elements behave essentially elastically over the timescales considered here. All elements below the elastic lithosphere have a lower viscosity value, appropriate for an asthenosphere. These elements experience viscous relaxation over time. Material property values adopted in our calculations are listed in Table 2. Parameters such as density and Young's modulus differ for the crust and mantle. Elements above depth t_c are assigned crustal values for these parameters; below this depth mantle values are assigned. Somewhat arbitrarily, for models discussed here, we have chosen $T_e = t_c$. We do not mean to imply that thicknesses of the Martian lithosphere and crust coincide; this choice serves only to simplify the model. The results of three computations are discussed here, with T_e values of 20, 40, and 80 km. These values chosen for T_e fall within the range discussed in *Comer et al.* (1985) for the Tharsis Montes and Olympus Mons. For $T_e = 20$ and 40 km, the outer radial boundary of the grid is taken as $r_{\max} = 1140$ km. For $T_e = 80$ km, such a value was found to be too small to avoid end effects, so we took $r_{\max} = 1600$ km.

In order to model plate flexure correctly, we must include the effect of buoyant support of the crust by the denser material beneath it. In TECTON, this is accomplished through the use of Winkler restoring forces at the nodes marking the boundary between the crust and the mantle (at a depth t_c). These Winkler forces are proportional to displacement. The buoyant force (per unit area) exerted by the mantle on the plate is:

$$f_b = -\rho_m g \ \delta z$$

where ρ_m is the mantle density, g is the gravitational acceleration (3.7 m/s^2), and δz is the vertical displacement. We specify Winkler forces of this magnitude at each node along the crust-mantle interface (applied over the appropriate area for that particular node).

The calculations performed here should be regarded as simple numerical experiments designed to explore the stress field resulting from a volcano-like load on an elastic plate underlain by a viscoelastic substrate. When applying the results of these calculations to actual geologic and tectonic features seen on Martian volcanoes, one must keep in mind the limitations of such models. The first and perhaps most important limitation is the instantaneous placement, at time $t = 0$, of a fully developed volcanic edifice. This simplification implies a volcano growth time t_g much less than the mantle Maxwell time τ_M. For Mars, if $\eta \sim 10^{21}$ Pa-s and $\mu \sim 10^{11}$ Pa, $\tau_M \sim 10^{10}$ s or 300 yr. The condition $t_g << \tau_M$ is thus clearly unrealistic. The effect of episodic increments to load size (due to episodic eruptions) over many Maxwell times are not amenable to investigation with this approach. In addition, even for the assumption of an instantaneous load, it is difficult to determine appropriate values for the initial geometry of a given volcano, since existing data apply only to volcanoes that have already undergone flexure and deformation that may have significantly modified initial conditions. These calculations are performed under the assumption of axial symmetry; possible effects of nonaxisymmetric loading (such as regional stress) and complex three-dimensional geometry are not incorporated. The effects of magma pressure, transport, and evacuation are not addressed in these preliminary models; these processes likely have important influences for caldera and flank tectonic evolution (*Thomas et al.*, 1990; *Zuber and Mouginis-Mark*, 1990). Further, lateral variations in material properties (due to horizontal temperature gradients, for example) are not included. Our choice that $T_e = t_c$, while made for convenience, is not necessarily valid for the Tharsis region. Finally, it must be remembered that once faulting occurs, the stress fields calculated are no longer strictly valid, since faulting would relieve stresses locally and could thus alter the predictions for failure at subsequent times. As discussed below, some of these limitations can be relaxed in future modeling efforts.

NUMERICAL RESULTS: STRESS, DEFORMATION, AND FAULTING

The evolution of the stress field within and beneath the volcanic edifice in a model is dipicted by means of symbols for the principal stresses within each element (Figure 7). The hourglass shapes are oriented along directions of deviatoric compression, while the bars are oriented along directions of deviatoric tension; symbol dimension is proportional to stress magnitude. For a general state of stress in a plane layer (without the volcanic load), the orientation of the stress symbol will be as in Figure 7: maximum compression vertical and maximum extension horizontal. The magnitude of the deviatoric stress will increase with depth. For a medium constrained laterally, this result can be derived from the equations for uniaxial strain (compaction) in the z-direction (e.g., *Turcotte and Schubert*, 1982 , p.108):

$$\sigma_{rr} = \sigma_{\theta\theta} = \left(\frac{\nu}{1-\nu}\right)\sigma_{zz}$$

For $\nu = 0.25$, the factor $\nu/(1 - \nu)$ is 1/3. Thus, the vertical stress will be three times as great as the horizontal stress, and with vertical stress equal to the overburden stress ($\sigma_{zz} = \rho_c g z$), the stress difference will increase with depth.

One such model for the evolution of volcano-related stresses is shown in Figure 8. At $t = 0$ (Figure 8a) deviatoric stresses display the orientations and magnitudes expected from simple self-loading of horizontal layers everywhere but along the top layer of volcano elements, where the stresses are rotated such that the compressive axis is almost horizontal. As the effects of flexure manifest themselves, this rotation propagates deeper into the volcano, eventually reaching the upper part of the underlying plate (Figure 8b-d).

The evolution of surface elevation, relative to its value at the right boundary $r = r_{max}$, is shown as a function of time in Figure 9, for computations with three different values of T_e. For all cases, most of the subsidence takes place between 10 and 100 Maxwell times. The maximum amount of subsidence occurs over the center of the volcanic load. This subsidence results in a reduction of volcano slope with time. Table 3 lists the average volcano slope for each of our computations for the elastic solution and as a function of time. The slope for the assumed initial volcano has a value of 6.34°. The amounts of subsidence and slope change increase with decreasing plate thickness.

The magnitudes of the surface stresses σ_{rr}, and $\sigma_{\theta\theta}$ are shown as functions of time in Figure 10. The stresses depicted are actually calculated at the center of each linear quadrilateral element at the surface of the model. The jaggedness in the curves occurs because the depth of the top elements changes along the slope of the volcano.

Given stress values, we may use the Mohr-Coulomb failure criterion to estimate regions where faulting would occur. The Mohr-Coulomb failure equation relates shear stress τ at failure to normal stress σ_n

$$\tau_{\mathrm{failure}} = c + \sigma_n \tan \phi$$

where c is the cohesive strength of the rock and ϕ is the angle of internal friction of the rock. We adopt values for c ($3.8\mathrm{x}10^7$ Pa) and ϕ (49°) appropriate for basalt (*Handin*, 1966). Once we have found where failure is expected, the orientations of principal stresses are used to determine the style and orientation of faulting, according to the criteria set forth by *Anderson* (1951). Given the directions of the horizontal and vertical normal stress components, the type of faulting (normal, thrust, or strike-slip) and the orientation (radial or circumferential) can be determined. Table 4 gives a listing of the possible types and orientations of faulting resulting from given stresses. Here σ_1 refers to the greatest compressive stress, σ_3 to the greatest extensional stress. Elements where failure predicted to have occurred are assigned a symbol corresponding to the stress state at that node. This classification scheme holds if the principal stresses approximately correspond to the horizontal (σ_{rr}, $\sigma_{\theta\theta}$) and vertical stresses (σ_{zz}) listed here. If the stresses are not aligned in this way, the asterisk symbol is assigned. Strike-slip faults do not quite fit the usual definitions of radial and circumferential, because such faults strike obliquely to the principal stress directions. For most rocks, strike-slip faults make smaller angles with the σ_1 than the σ_3 direction. Thus, when $\sigma_1 = \sigma_{\theta\theta}$ we will consider the resulting faults circumferentially oriented, and when $\sigma_1 = \sigma_{rr}$ we consider them radial. Care must be taken when applying these results to regions at depth, or where principal stresses are rotated obliquely to the surface. For the purposes of applying the categorization of Table 4, principal stresses making angles of less than 20° with the horizontal are considered horizontal, and similarly for near vertical stresses.

The predicted locations and types of faulting as functions of time are shown in Figures 11-13 for the three values of elastic lithosphere thickness. Figure 11 depicts the case with $T_e = 40$ km. After 10 Maxwell times (Figure 11a), a region of failure has initiated near the outer edge of the volcano surface. This region exhibits mostly circumferential normal faulting, with a small section of circumferential strike-slip faulting toward the volcano. After 100 Maxwell times (Figure 11b), this region expands dramatically. Two new zones of failure also appear: a zone of thrust faulting along the upper flank, and a region of normal faulting of an average depth of 30 km beneath the center of the volcanic load. The predicted fault orientation on the flanks is predominantly circumferential, but a radial orientation is predicted for a small annulus approximately midway downslope. The region of subsurface faulting lies between 20 and 40 km depth and extends laterally beyond the outer volcano radius. It consists of a core region of circumferential normal faulting, surrounded by a region of radial normal faulting. After 1000 Maxwell times (Figure 11c), little change is evident other than a slight outward extension of the surficial region of normal faulting and a greater volume of mixed fault geometry in the subsurface faulting region.

Changing the plate thickness can affect the evolution of failure regions. For $T_e = 20$ km, failure is predicted in only one element after 10 τ_M (Figure 12a). After 100 τ_M (Figure 12b), regions of faulting similar in location and style to those in Figure 11b appear, with the modifications that the region of strike-slip faulting is shifted inward and up the volcano flank, the region of surficial normal faulting is smaller in extent, and the region of subsurface normal faulting is shallower (10-20 km deep). Also, the subsurface normal faulting region takes longer to extend beyond the volcano radius (Figure 12b).

Results for the computation with $T_e = 80$ km also reveal interesting changes. At $t = 10\ \tau_M$ (Figure 13a), the only faulting occurs at the surface, at the edge of the volcano. At $t = 100\ \tau_M$ (Figure 13b), flank thrust faulting is predicted, similar to that in Figure 11b. The subsurface faulting region is found at a deeper level (60-80 km depth). The outer faulting region shows the most dramatic change from the calculations with thinner lithospheres. This region expands outwards to more than two volcano radii from the center, as well as down to a maximum depth of 20 km. Circumferential strike-slip faulting is much more prominent than in the previous cases, and is farther from the volcano. Finally, at $t = 1000\ \tau_M$ (Figure 13c), we observe that the outer region of faulting has migrated even farther, out to a maximum extent of three volcano radii from the center, and that the area undergoing strike-slip faulting has grown slightly.

DISCUSSION: IMPLICATIONS FOR VOLCANO EVOLUTION

The volcanic edifice stress fields calculated here have important implications for magma transport and eruption. Magma propagates through fractures that form perpendicular to the direction of least compressive stress. The elastic solution (Figure 8a) clearly shows that magma can propagate vertically, with a clear path to the summit caldera. As a result of flexure, however, the principal stress directions in the edifice rotate such that the most compressive stress is horizontal. In this region, the magma propagation direction should tend to the horizontal, leading outward from the summit to the flanks. Thus an implication of the models treated here is that there should be an evolution in favored eruption location from summit to flank. Such an evolution is consistent with the first two stages in the sequence of major events for the Tharsis Montes determined by *Crumpler and Aubele* (1978).

The predicted types and orientations of faulting in our models (Figures 11-13) can be compared with observed features on and around the Tharsis volcanoes. Circumferential graben are observed on the lower flanks and the surrounding plains for all three of the Tharsis Montes (Figures 2-5). An interpretation of the basal scarp of Olympus Mons as a large-offset listric normal fault (*Francis and Wadge*, 1983) is also consistent with model results. Circumferential terraces high on the flanks of Olympus have been interpreted as concentric thrust faults by *Thomas et al.* (1990), who applied elastic finite element models to investigate edifice stresses and deformation. Interestingly, our models indicate that these faults would form only as a result of flexural stress, whereas the models of Thomas and coworkers do not include flexural stresses, but suggest that purely elastic stresses are sufficient to exceed the compressive failure strength at near surface conditions. The thrust faulting region in our model is somewhat difficult to reconcile with the observation of graben rather high on the slopes of Arsia and Pavonis Mons (Figures 4, 5). Clearly, an extensional environment existed in the upper volcano flanks at some time in the evolution of these constructs. These graben may be related, however, to faulting beneath the volcano, as discussed below.

Linear symmetries observed in all the Tharsis Montes volcanoes may be indirect evidence for failure in the sub-volcano region. The second stage in the *Crumpler and Aubele* (1978) sequence of volcano evolution involves the development of a linear rift bisecting the volcanoes, with eruptions emanating from this rift. Radially oriented normal faulting under a volcano might be thought at first to tend to divide the volcano into radial sections, much like pie slices. The above evidence, however, suggests that this mode of failure may be concentrated into one large linear feature that bisects the volcano. This feature may owe its orientation to regional stress fields or to pre-existing zones of weakness. Our calculations predict radially oriented normal faulting in a broad zone beneath a volcano. For the case with $T_e = 20$ km (Figure 12), this zone extends beyond the volcano radius and reaches quite close to the surface. Such a zone, if concentrated into a linear feature and if continued to the surface by sustained faulting, may give rise to the linear rifts and bilateral symmetry observed on the Tharsis Montes.

The evolution of Pacific hotspot volcanoes may provide some insight into the formation and influence of a bisecting rift zone. For instance, *Holcomb* (1985) has suggested that the island of Molokai in the Hawaiian chain resembles a volcano cut almost exactly in half, with one part transported downslope in a massive submarine slide, and the other part remaining to form the present island. Bathymetry of the ocean floor north of Molokai (*Moore*, 1964) supports this conclusion. We conjecture that a similar but less extreme mechanism could explain the presence of graben on the upper slopes of Arsia Mons and Pavonis Mons, in that as the volcano halves slide apart from each other, an extensional environment is created near the summit. To fully investigate this possibilty, a fully three dimensional model, or an axisymmetric model with non-axisymmetric loading, is required.

We should also note that there are features predicted in our calculations that have no observable counterparts on the Tharsis volcanoes. In particular, evidence for strike-slip faulting around any of these structures is lacking. For values of lithosphere thickness appropriate to the Tharsis Montes, however, the zone of predicted strike-slip faulting lies at the edge of the volcanic construct, which has the lowest surface elevation (Figure 9). This topographic low could accumulate lava flows and erosional deposits which would cover the strike-slip zone, hiding it from photographic surveys. Alternatively, since the preferred initial failure mode for all except a very narrow annulus is concentric normal faulting, perhaps the initially formed faults continue to accommodate release of stress at subsequent stages in the development of flexure. Evidence for radially oriented thrust faulting has also not been observed on the lower flanks of any of the Tharsis volcanoes. Obscuration of such faults by flank lava flows is a possible explanation. If the rifts bisecting the Tharsis Montes are actually zones of radial normal faulting from which both halves of the volcano have slid apart, as suggested above, then the propagation of the normal faulting zone to the surface could change the stress fields in the lower flanks, relieving the compressive stresses expected from our calculations.

The relative timing of events in our models is generally consistent with the chronology set forth by *Crumpler and Aubele* (1978) for the Tharsis Montes. After construction of the main shield, rift formation and flank eruptions along this rift occur in the second stage of evolution. Figure 8b shows that, after 10 Maxwell times, the principal model result is the beginning of rotation of the stress axes in the edifice (which is expected to favor flank eruptions). After a few tens of Maxwell times the failure zone beneath the volcano (which could favor formation of the rift) has begun to grow. The third stage involves summit subsidence and formation of concentric fractures and graben. After 100 Maxwell times, our computations show increased subsidence (Figure 9) as well as the growth of the region of normal faulting outwards of the volcano (Figure 11b). The fourth stage involves further eruption along the rift, flooding the summit and flanks. Late stage flank eruptions are consistent with the stress fields in our calculations. Summit eruptions, however, would not be favored by the computed stress fields. It is likely that the stress field is influenced by the effects of previous stages of the evolution. Flank eruptions result in an added flank load, not modelled here, to which the lithospere will respond with additional flexure. Subsidence and additional flexure near the flanks of the volcano may at least partially relieve the compressional stresses near the summit, thus enhancing the possibility of additional summit eruptions. By this scenario, the preferred site for eruptions could alternate between summit and flank, on time scales on the order of 100-1000 τ_M. Also, the effect of sections of the volcano sliding away from the bisecting rift may result in an extensional environment near the summit, once again favoring summit eruptions.

Realizing the limitations of these calculations in accurately modeling the behavior of large volcanoes, we hope to be able to relax some of these limitations in future models. The restriction of small volcano growth time t_g can be removed with incremental loading, a capability which requires code development. Such a capability can also permit investigation of the effects of flexure on modulating eruption timing and location. A study of the effects of faulting on volcanic displacements and stresses can be accomplished through existing provisions in TECTON for modeling fault discontinuities, by means of the slippery node method (*Melosh and Williams*, 1989).

CONCLUSIONS

In this paper we have used finite element calculations that simulate the effects of lithospheric flexure to investigate the deformation and stress histories resulting from a volcano load on the lithosphere. The results of these calculations are compared with observed tectonic features and inferred eruption characteristics of large Martian volcanoes. Some of the zones of failure and faulting predicted in our models have direct analogues in observed features; others may be indirectly related to actual structures. Three regions of failure with characteristic stress regimes are identified in our calculations. Stresses caused by flexure and subsidence may lead to thrust faulting on the flanks of large volcanoes. Flexural stresses in the lithospere immediately surrounding the volcano can result in circumferential graben. Flexurally induced failure in a wide zone beneath the center of a large volcano may play a major role in the development and modification of the edifice. Given that magma propagates perpendicular to the least compressive stress, a rotation in the principal stress orientations during lithospheric flexure in the models tends to favor eruption sites shifting from the volcano summit to the flanks as flexure proceeds. We conclude that time-dependent lithospheric flexure is important in determining the location and style of faulting within and surrounding large volcanoes as well as regulating the timing and location of volcanic eruptions.

ACKNOWLEDGMENTS

We thank Jay Melosh for generously providing us a copy of the TECTON code and for instructing us in its use. Steve Squyres and Andrea Borgia provided preprints of their papers prior to publication. Bob Grimm, Buck Janes, and Ken Tanaka offered helpful comments on an earlier draft. This research was supported by the NASA Planetary Geology and Geophysics Program under grants NAGW-1077 and NAGW-1937.

REFERENCES

Anderson E. M. (1951) *The Dynamics of Faulting and Dyke Formation with Applications to Britain.* 2nd ed., Oliver and Boyd, Edinburgh. 206 pp.

Blasius K. R. and Cutts J. A. (1976) Shield volcanism and lithospheric structure beneath the Tharsis plateau, Mars. *Proc. Lunar Planet. Sci. Conf. 7th,* 3561-3573.

Blasius K. R. and Cutts J. A. (1981) Topography of Martian central volcanoes. *Icarus, 45*, 87-112.

Borgia A., Burr J., Montero W., Alvarado G. E., Morales, L. D., and Alvarado, G.E. (1990) Fault-propagation folds induced by gravitational failure and slumping of the Central Costa Rica volcanic range: Implications for large terrestrial and Martian volcanic edifices. *J. Geophys. Res., 95,* 14357-14382.

Chevallier L. and Verwoerd W. J. (1988) A numerical model for the mechanical behavior of intraplate volcanoes. *J. Geophys. Res., 93*, 4182-4198.

Comer R. P., Solomon S. C., and Head J. W. (1985) Mars: Thickness of the lithosphere from the tectonic response to volcanic loads. *Rev. Geophys., 23*, 61-92.

Crumpler L. S. and Aubele J. C. (1978) Structural evolution of Arsia Mons, Pavonis Mons, and Ascraeus Mons: Tharsis region of Mars. *Icarus, 34*, 496-511.

Dieterich J. H. (1988) Growth and persistence of Hawaiian volcanic rift zones. *J. Geophys. Res., 93*, 4258-4270.

Francis P. W. and Wadge G. (1983) The Olympus Mons aureole: Formation by gravitational spreading. *J. Geophys. Res., 88,* 8333-8344.

Greeley R. and Spudis P.D. (1981) Volcanism on Mars. *Rev. Geophys. Space Phys., 19*, 13-41.

Handin J. (1966) Strength and ductility. In *Handbook of Physical Constants* (edited by S.P. clark, Jr.), *Memoir 97.* Geol. Soc. Amer., Boulder, Colo., pp. 223-289.

Harris S. A. (1977) The aureole of Olympus Mons, Mars. *J. Geophys. Res., 82*, 3099-3107.

Holcomb R. T. (1985) The caldera of East Molokai volcano, Hawaiian Islands. In *National Geographic Society Research Reports (for 1980-1983), 21*, 81-87.

Lopes R. M. C., Guest J. E., and Wilson C. J. (1980) Origin of the Olympus Mons aureole and perimeter scarp. *Moon Planets, 22*, 221-234.

McNutt M. K. (1984) Lithospheric flexure and thermal anomalies. *J. Geophys. Res., 89*, 11180-11194.

Melosh H. J. and Rafesky A. (1980) The dynamical origin of subduction zone topography. *Geophys. J. R. Astron. Soc., 60*, 333-354.

Melosh H. J. and Rafesky A. (1983) Anelastic response of the Earth to a dip slip earthquake. *J. Geophys. Res., 88*, 515-526.

Melosh H. J. and Williams C. A., Jr. (1989) Mechanics of graben formation in crustal rocks: A finite element analysis. *J. Geophys. Res., 94*, 13961-13973.

Moore J. G. (1964) Giant submarine landslides on the Hawaiian ridge. *U. S. Geol. Survey Prof. Paper 501-D*, pp. D95-D98.

Morris E. C. (1981) The basal scarp of Olympus Mons (abstract). *Reports of the Planetary Geology Program-1988, NASA TM 84211*, 389-390.

Ryan M. P. (1988) The mechanics and three-dimensional internal structure of active magmatic systems: Kilauea volcano, Hawaii. *J. Geophys. Res., 93*, 4213-4248.

Scott D. H. and Tanaka K. L. (1981) Map showing lava flows in the northeast part of the Phoenicis Lacus quadrangle of Mars. Map I-1277, U. S. Geol. Surv., Reston, Va.

Scott D. H., Schaber G. G., Horstmann K. C., Dial A. L., Jr., and Tanaka K. L. (1981a) Map showing lava flows in the southwest part of the Tharsis quadrangle of Mars. Map I-1268, U. S. Geol. Surv., Reston, Va.

Scott D. H., Schaber G. G., and Tanaka K. L. (1981b) Map showing lava flows in the southeast part of the Tharsis quadrangle of Mars. Map I-1269, U. S. Geol. Surv., Reston, Va.

Scott D. H., Schaber G. G., Horstmann K. C., Dial A. L., Jr., and Tanaka K. L. (1981c) Map showing lava flows in the northwest part of the Phoenicis Lacus quadrangle of Mars. Map I-1272, U. S. Geol. Surv., Reston, Va.

Solomon S. C. and Head J. W. (1990) Heterogeneities in the thickness of the elastic lithosphere of Mars: Constraints on heat flow and internal dynamics. *J. Geophys. Res., 95*, 11073-11083.

ten Brink, U. S. and Brocher T. M. (1987) Multichannel seismic evidence for a subcrustal intrusive complex under Oahu and a model for Hawaiian volcanism. *J. Geophys. Res., 92*, 13687-13707.

Tanaka K. L. (1986) The stratigraphy of Mars. *Proc. Lunar Planet. Sci. Conf. 17th*, in *J. Geophys. Res., 91*, E139-E158.

Thomas P. J., Squyres S. W., and Carr M. H. (1990) Flank tectonics of Martian volcanoes. *J. Geophys. Res., 95*, 14345-14355.

Thurber C. H. and Gripp A. E. (1988) Flexure and seismicity beneath the south flank of Kilauea volcano and tectonic implications. *J. Geophys. Res., 93*, 4271-4278.

Turcotte D. L. and Schubert G. (1982) *Geodynamics*. Wiley, New York. 450 pp.

Wu, S. S. C. (1978) Mars synthetic topographic mapping. *Icarus, 33*, 417-440.

Wu S. S. C., Garcia P. A., Jordan R., Schafer F. J., and Skiff B. A. (1984) Topography of the shield volcano, Olympus Mons on Mars. *Nature, 309*, 432-435.

Zuber M. T. and Mouginis-Mark P. J. (1990) Constraints on the depth and geometry of the magma chamber of Olympus Mons volcano, Mars (abstract). In *Lunar and Planetary Science XXI*, pp. 1387-1388. Lunar and Planetary Institute, Houston.

FIGURE CAPTIONS

Figure 1. Viking Orbiter view of Olympus Mons. The multiple pit caldera and basal scarp (at bottom) are the main tectonic features visible. No graben are seen on the flanks of the volcano or on the volcanic plains immediately surrounding the structure. Frame VO641A52; width of image is 440 km.

Figure 2. Viking orbiter view of western Ascraeus Mons. The complex caldera is seen at the summit, and graben with a predominantly circumferential orientation are seen along the western and southwestern margins. Graben are located on Ascraeus Mons itself and in surrounding flows (unit as, Figure 3). Frame VO643A78; width of image is 420 km.

Figure 3. Geologic map of Ascraeus Mons and surroundings, simplified from *Scott et al.* (1981b) by *Comer et al.* (1985). Volcanic units shown include relatively young Ascraeus Mons flows (as), intermediate-age Tharsis Montes flows (tm), and volcanic material undivided by age (vu). Also shown as a distinct unit is slide material (s), interpreted by Scott and coworkers as landslides and debris flows. Dashed lines show approximate elevation contours, in kilometers, relative to a fourth-degree, fourth-order equipotential (*Wu*, 1978). The summit caldera complex is indicated by inward hatched lines. Extensional faults and graben are shown as heavy lines.

Figure 4. Geologic map of Pavonis Mons and surroundings, simplified from *Scott et al.* (1981a, b, c) and *Scott and Tanaka* (1981) by *Comer et al.* (1985). Units shown, in addition to those described in Figure 3, are relatively young volcanic flows from Pavonis Mons (pm) and Arsia Mons (am). Other information follows the format of Figure 3. Circumferential graben reach quite far up the slopes, and an approximate bilateral symmetry can be seen about an axis trending approximately NNE-SSW.

Figure 5. Geologic map of Arsia Mons and surroundings, simplified form *Scott et al.* (1981c) by *Comer et al.* (1985). See Figures 3 and 4 for further explaination of symbols. Circumferential graben extend almost up to the summit caldera complex.

Figure 6. The finite element grid used for the calculations shown in later figures. The volcano is the small triangular area in upper left-hand corner.

Figure 7. Key for stress symbols in Figure 8. The hourglass shapes are oriented along directions of deviatoric compression, the bars along directions of deviatoric extension. Symbol size is proportional to stress magnitude. Magma is expected to propagate perpendicular to the least compressive stress.

Figure 8. Plots of deviatoric stresses in elements in the vicinity of the volcano, for the case with a 40 km elastic lithospere thickness. The hourglass shapes denote deviatoric compression, the bars deviatoric extension. (a) The elastic solution. (b-d) After 10, 100, and 1000 Maxwell times, respectively.

Figure 9. Plots of the elevation of the surface nodes of the model, relative to the surface node at the far end of the grid ($r = r_{max}$). (a) $T_e = 20$ km. (b) $T_e = 40$ km. (c) $T_e = 80$ km.

Figure 10. Plots of stresses calculated in the surface elements of the model, for the case with $T_e =$ 40 km. Stress is taken to be positive in extension. (a) The elastic solution. (b-d) After 10, 100, and 1000 Maxwell times, respectively. Note that the stress scale increases with each time increment.

Figure 11. A plot of the elements at which failure is predicted, giving the style and orientation of expected faulting. The lithosphere thickness is $T_e = 40$ km. (a-c) After 10, 100, and 1000 Maxwell times, respectively.

Figure 12. Plot of expected location and geometry of faulting versus time for $T_e = 20$ km. (a-c) After 10, 100, and 1000 Maxwell times, respectively.

Figure 13. Plot of expected location and geometry of faulting versus time for $T_e = 80$ km. (a-c) After 10, 100, and 1000 Maxwell times, respectively.

Table 1. Dimensions of Tharsis Volcanoes

Volcano	Diameter (km)	Relief (km)
Olympus Mons	600[a]	24[a]
Ascraeus Mons	400[b]	18[b]
Pavonis Mons	320[b]	14[b]
Arsia Mons	420[b]	19[c]

[a] *Wu et al.* (1984).

[b] *Blasius and Cutts* (1976).

[c] *Blasins and Cutts* (1981).

Table 2. Adopted Parameter Values

Parameter	Crust	Mantle
E, Pa	1×10^{11}	3×10^{11}
ρ, kg/m^3	3000	3500
ν	0.25	0.25

	Lithosphere	Asthenosphere
η, Pa s	1×10^{25}	1×10^{21}

Table 3. Average Slope Angles (in degrees)

T_e	Elastic	t=10 τ_M	t=100 τ_M	t=1000 τ_M
20 km	6.30	6.10	5.00	4.32
40 km	6.29	6.12	5.85	5.80
80 km	6.28	6.16	5.85	5.80

Table 4. Expected faulting types and symbols

σ_1	σ_3	style	orientation	Symbol
σ_{rr}	σ_{zz}	thrust	circumferential	t
σ_{rr}	$\sigma_{\theta\theta}$	strike-slip	radial	S
$\sigma_{\theta\theta}$	σ_{zz}	thrust	radial	T
$\sigma_{\theta\theta}$	σ_{rr}	strike-slip	circumferential	s
σ_{zz}	σ_{rr}	normal	radial	N
σ_{zz}	$\sigma_{\theta\theta}$	normal	circumferential	n
not aligned		mix	mix	*

Figure 1

Figure 2

ORIGINAL PAGE IS
OF POOR QUALITY

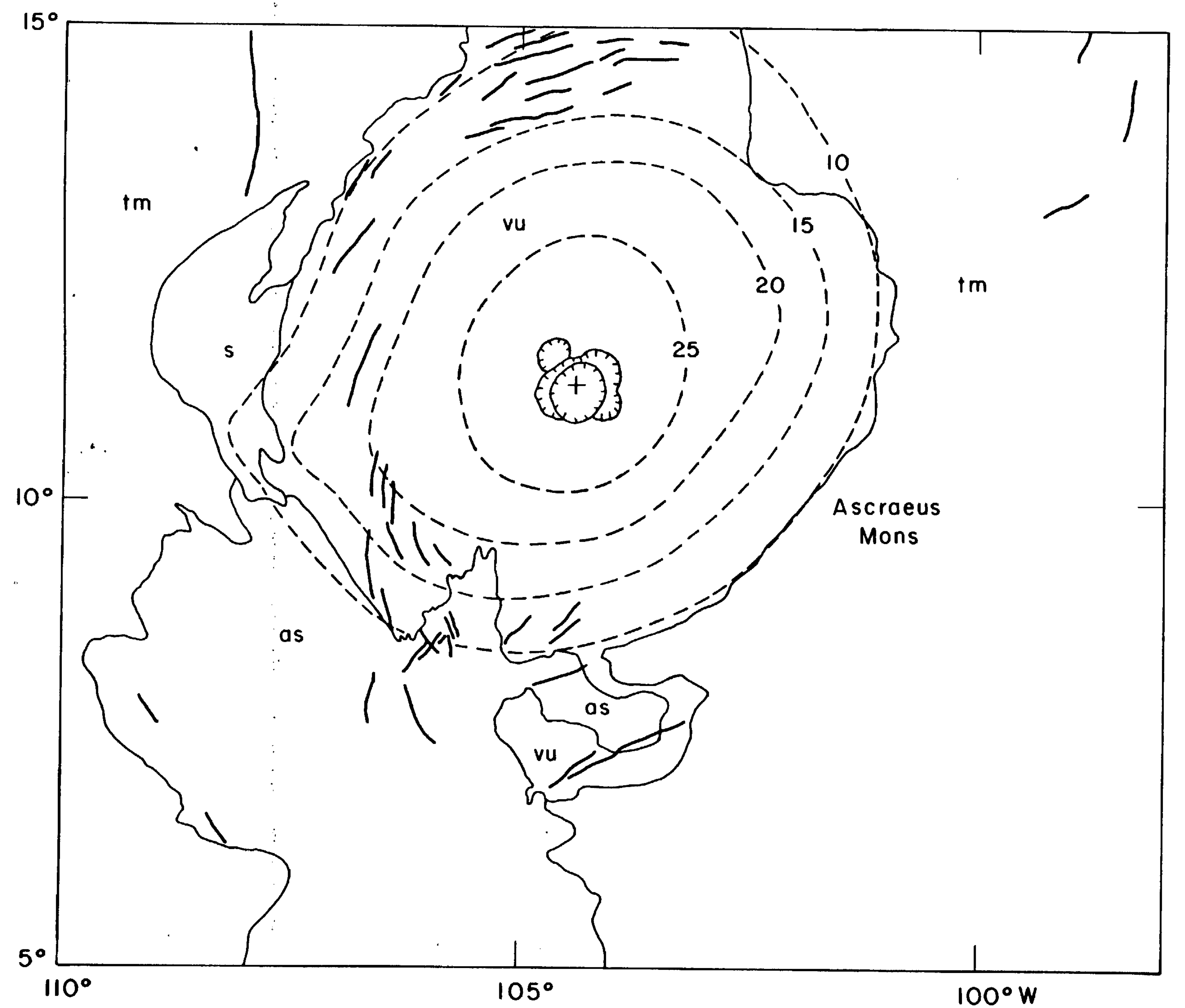
15°
10°
5°
110°
105°
100° W
tm
s
as
vu
10
15
20
25
tm
Ascraeus
Mons
as
vu

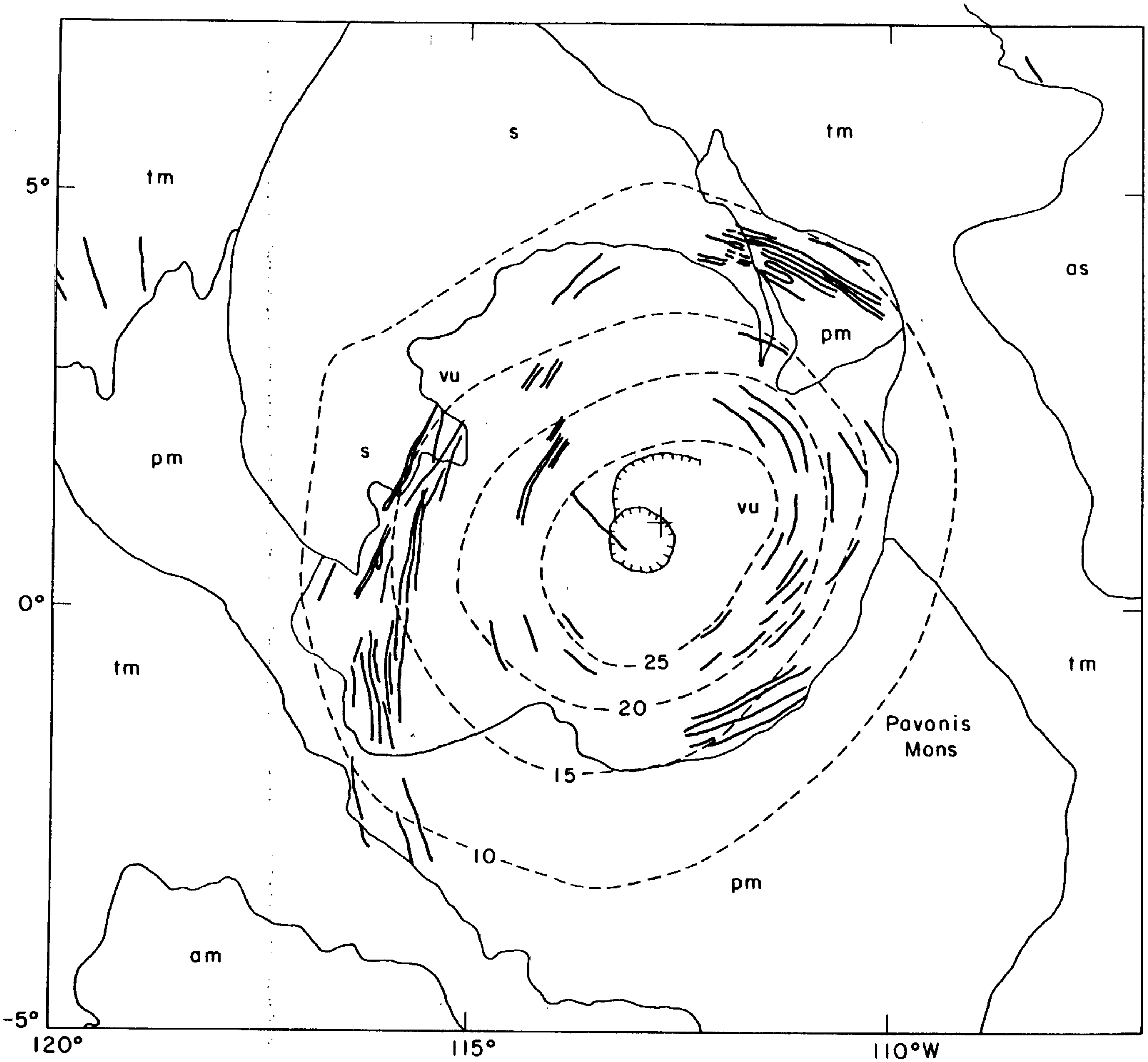
s
tm
tm
as
pm
vu
pm
s
vu
0°
5°
-5°
tm
tm
25
20
15
10
Pavonis
Mons
pm
am
120°
115°
110°W

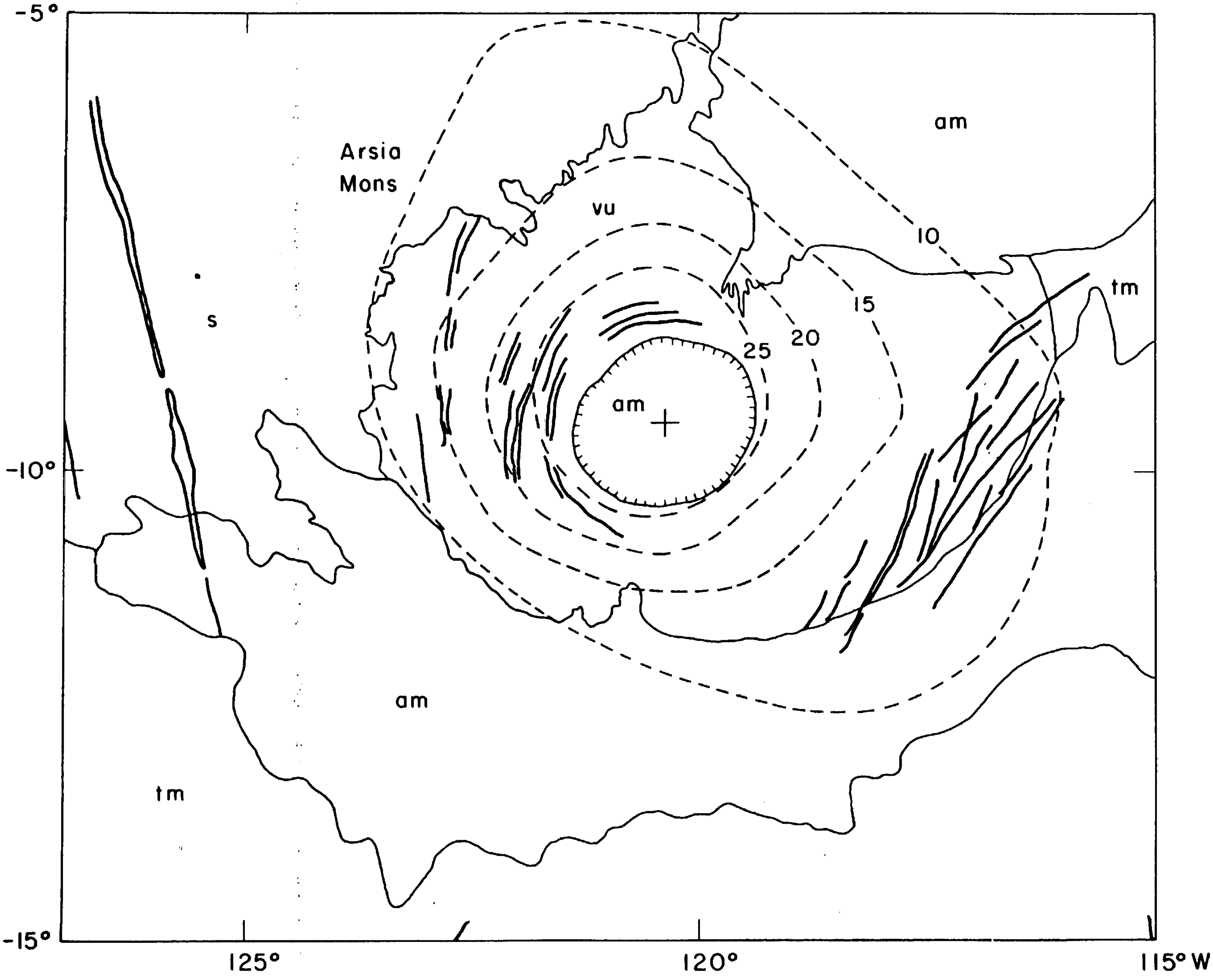
-5°
-10°
-15°
125°
120°
115° W
Arsia
Mons
am
vu
10
15
20
25
am
tm
s
am
tm

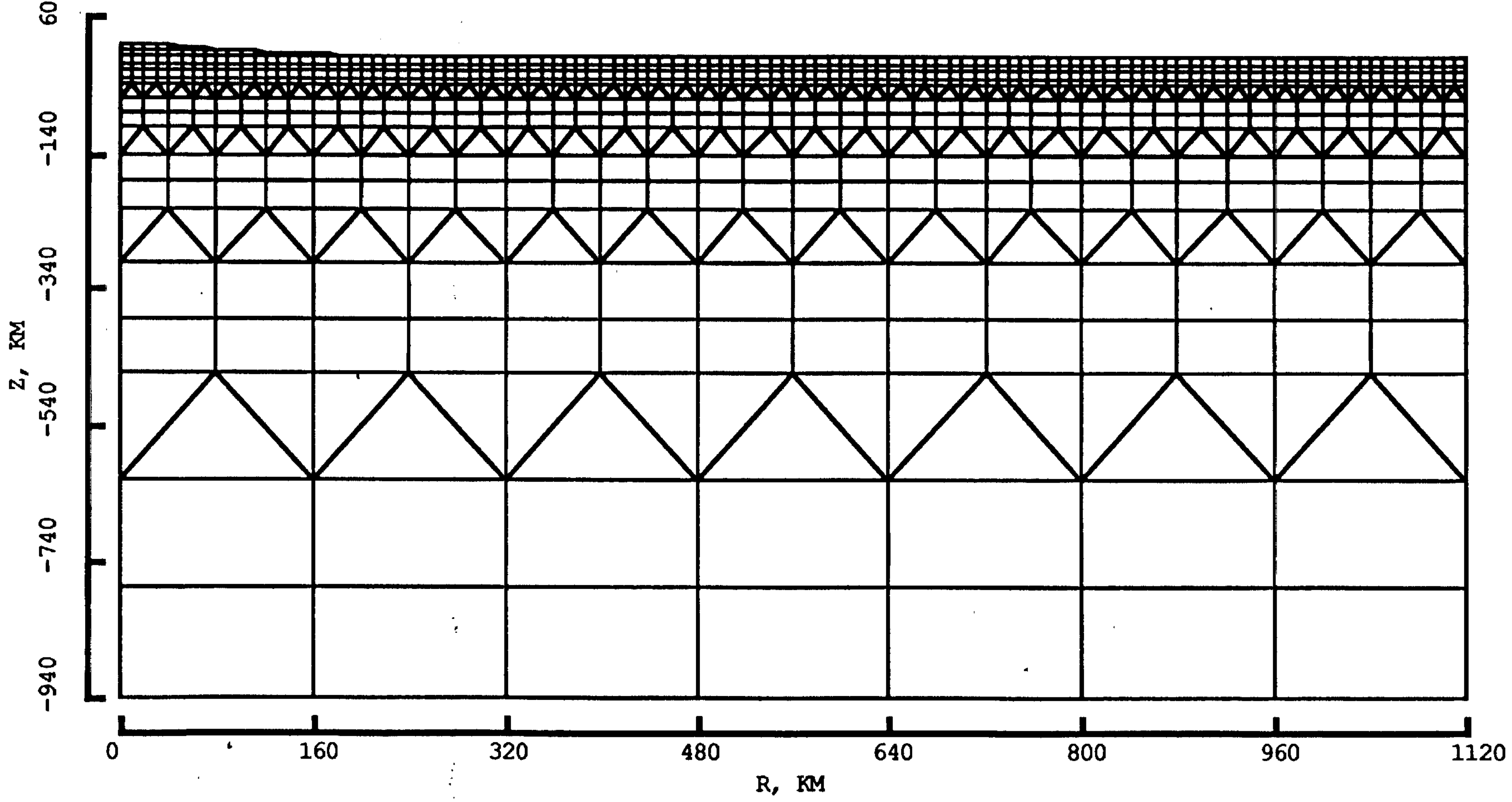

Figure 6

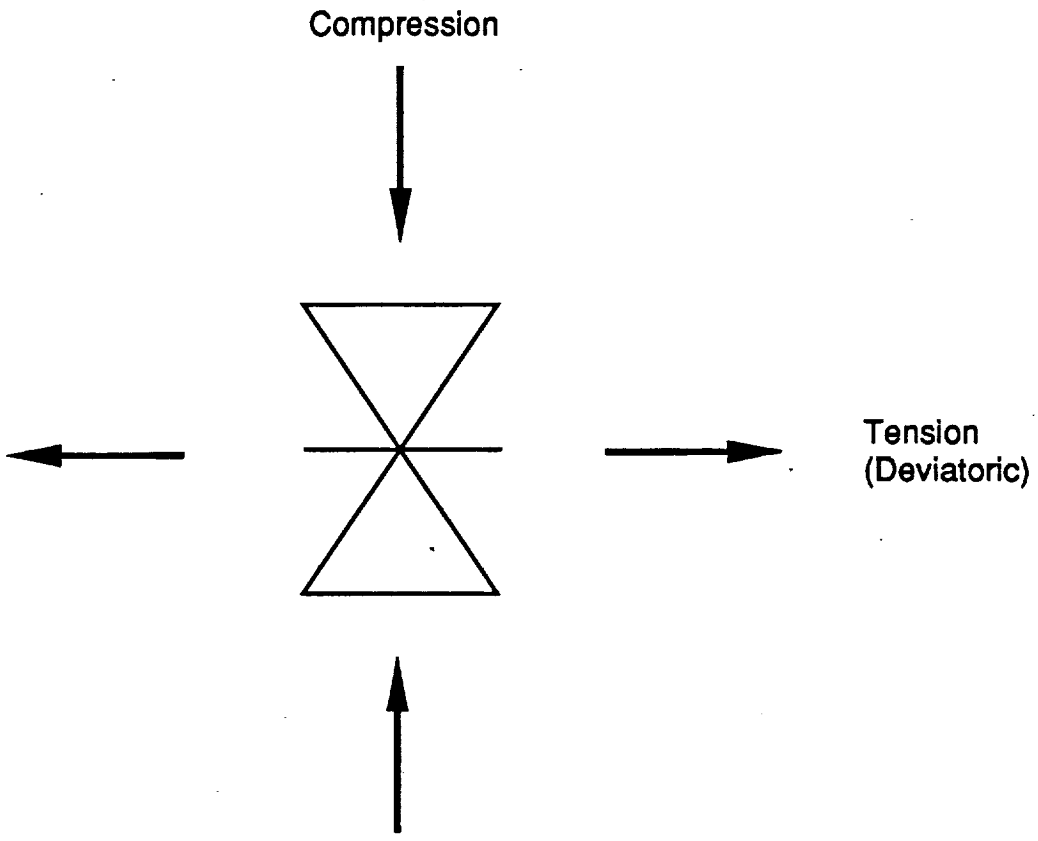

Figure 7

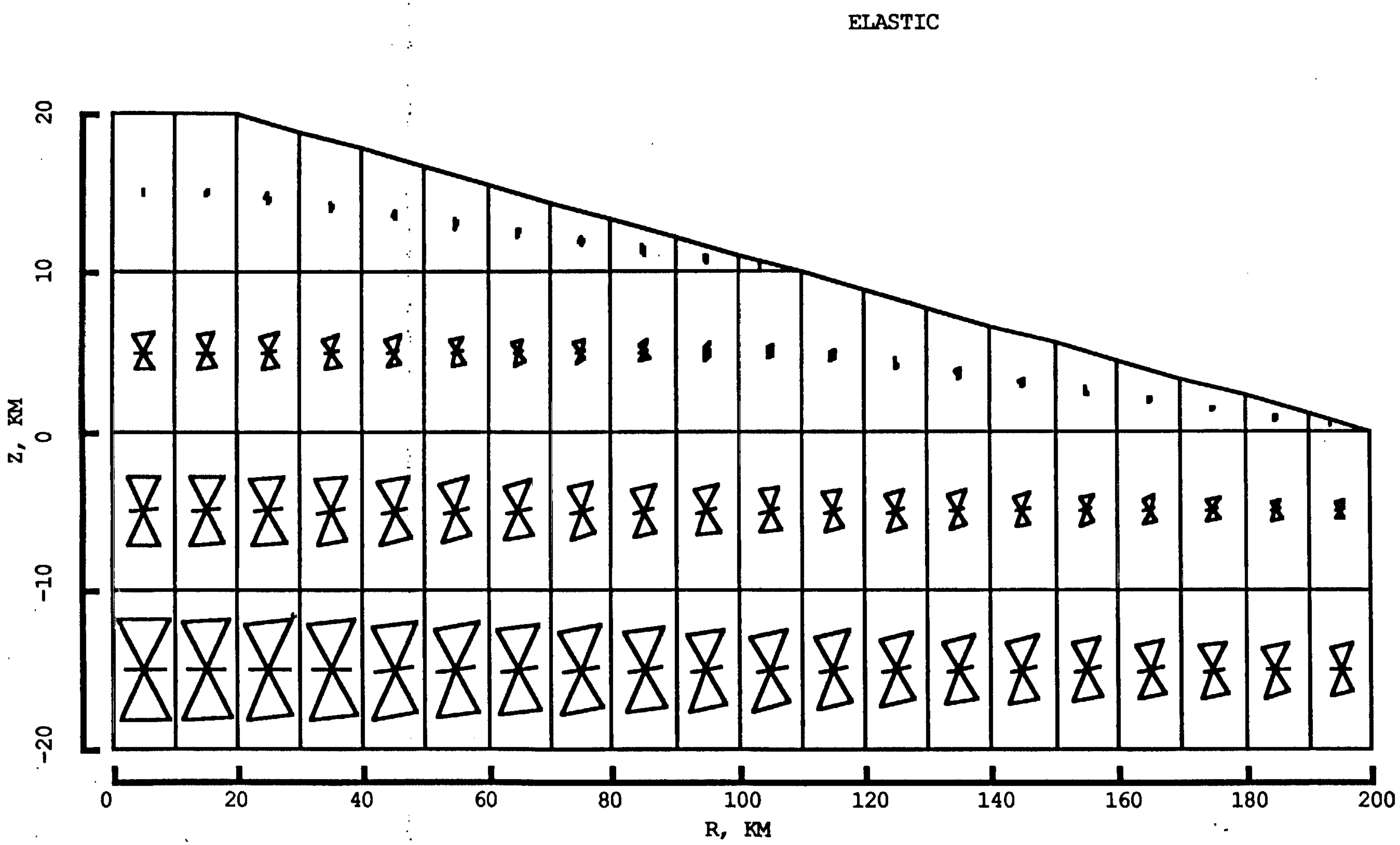

Figure 8a

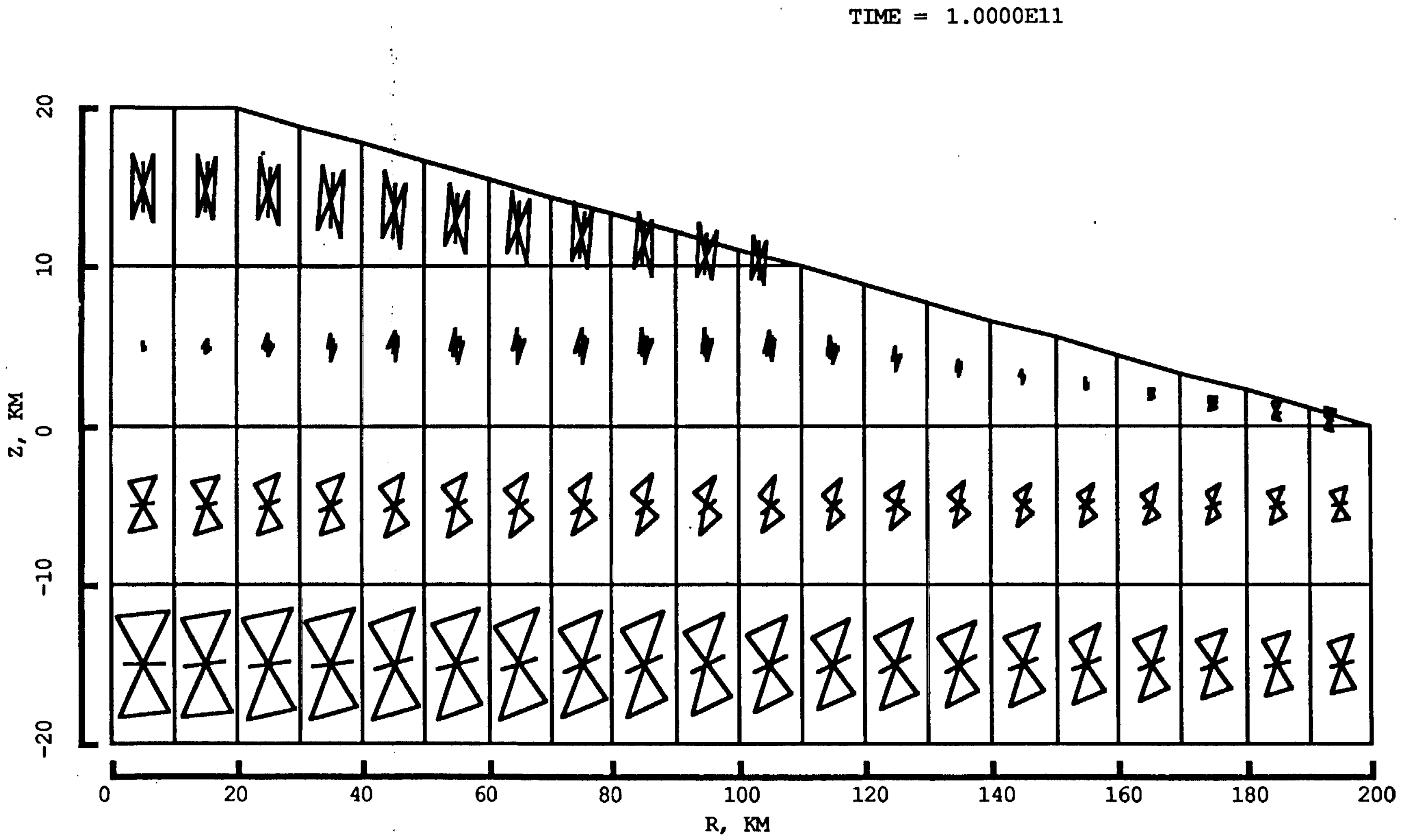
TIME = 1.0000E11
20
10
0
-10
-20
Z, KM
0
20
40
60
80
100
120
140
160
180
200
R, KM

Figure 8b

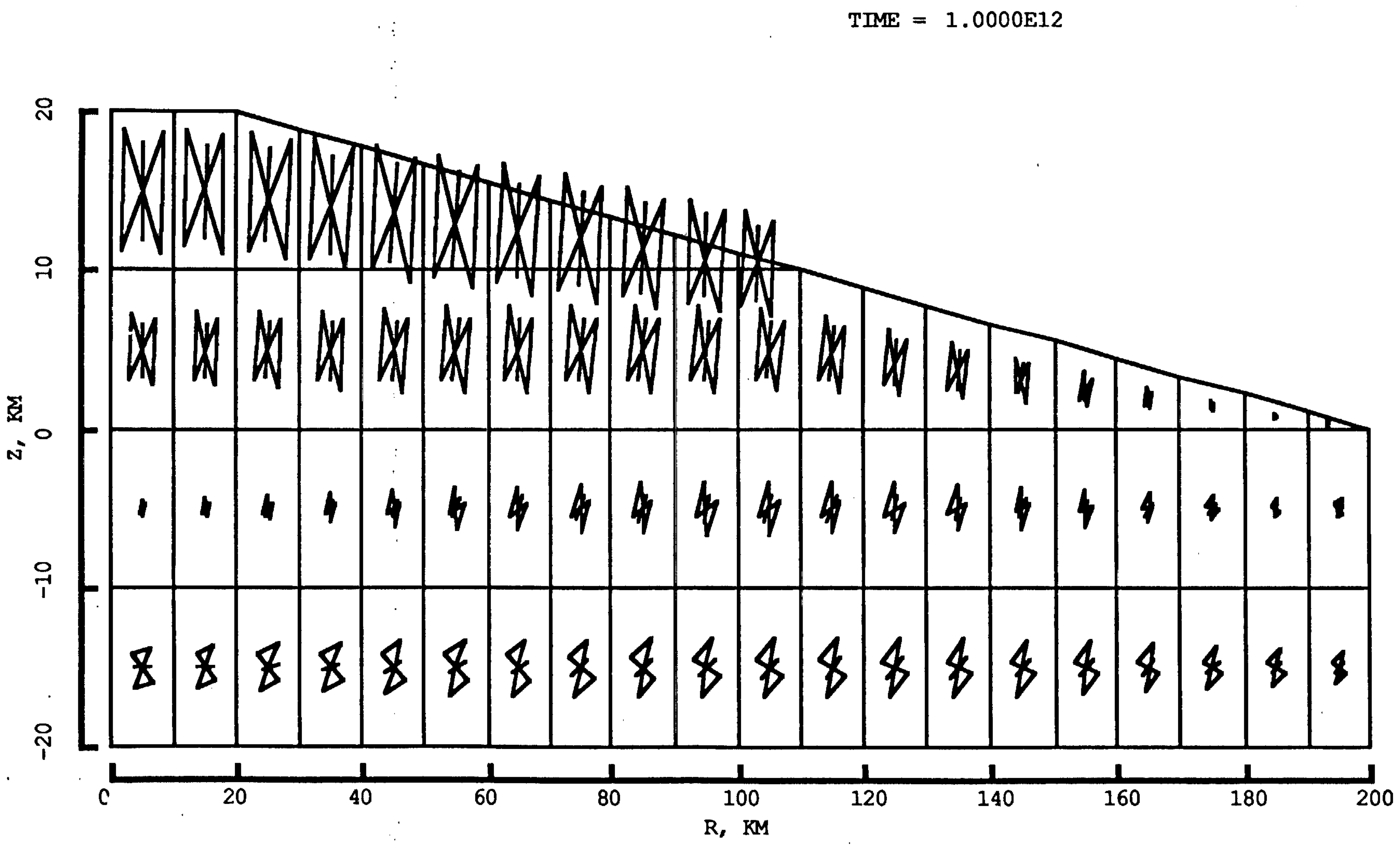
TIME = 1.0000E12
20
10
0
-10
-20
Z, KM
C
20
40
60
80
100
120
140
160
180
200
R, KM

Figure 8c

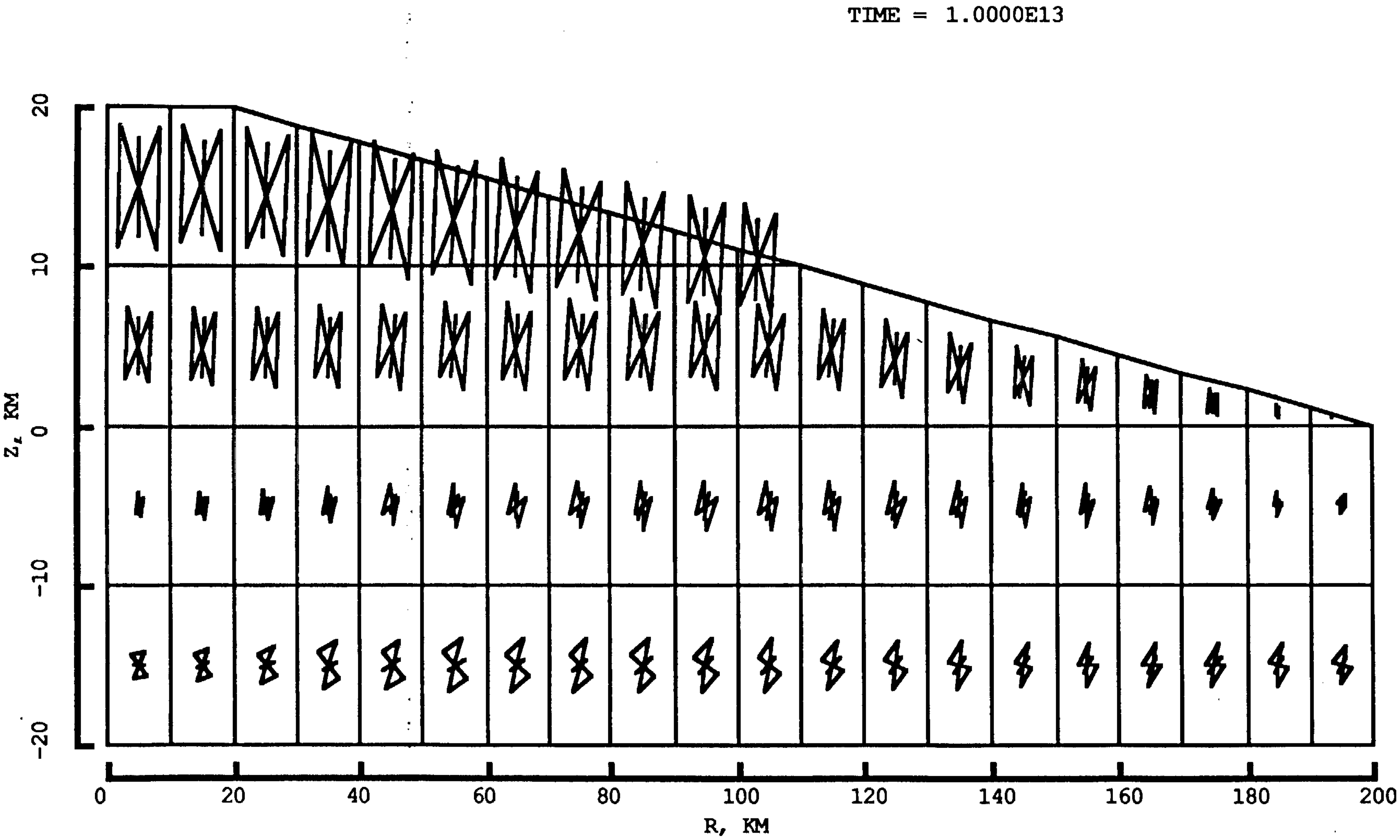
TIME = 1.0000E13
Z, KM
20
10
0
-10
-20
0
20
40
60
80
100
120
140
160
180
200
R, KM

Figure 8d

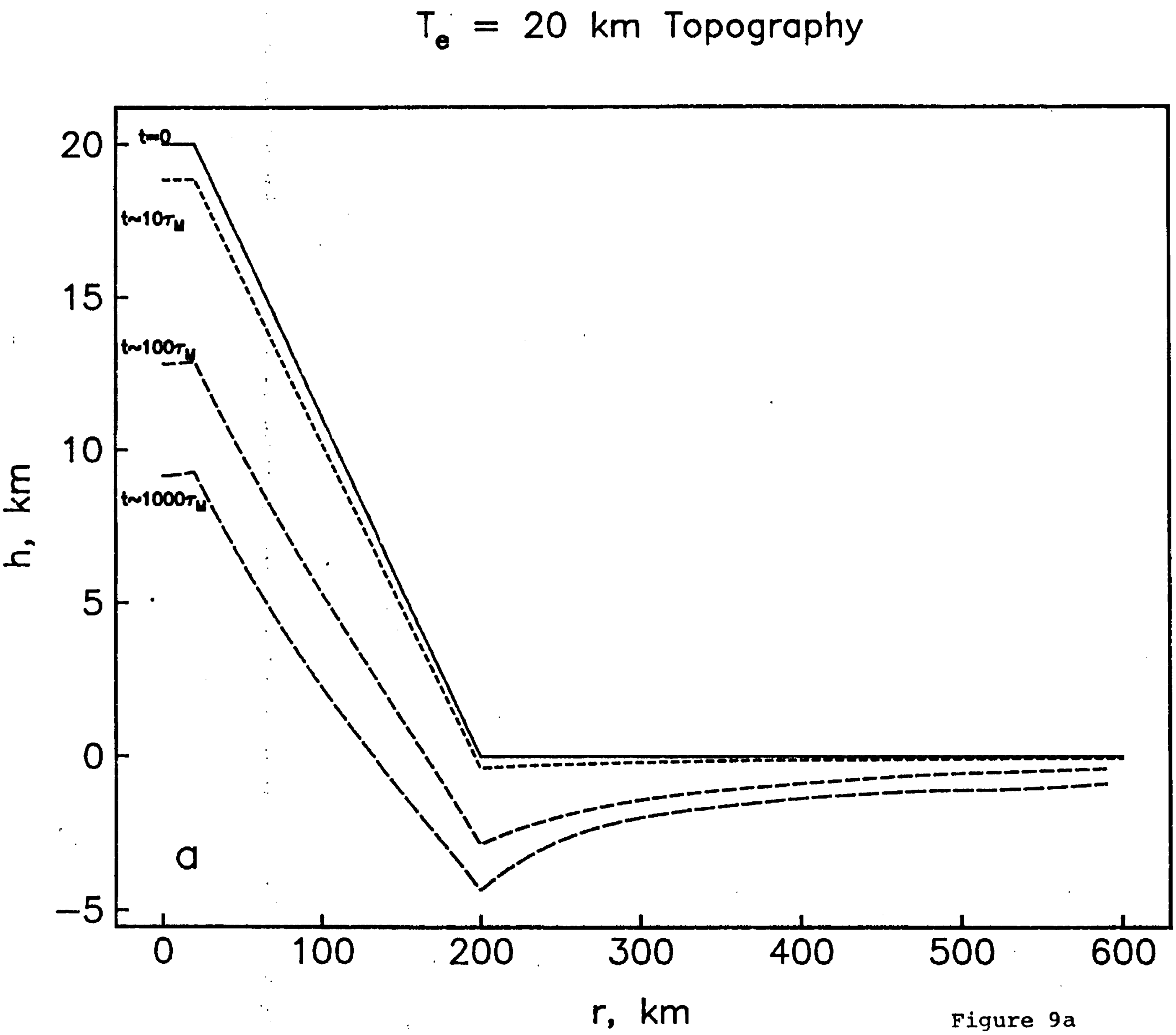
T_e = 20 km Topography
t=0
t~10τ_M
t~100τ_M
t~1000τ_M
a
h, km
20
15
10
5
0
−5
r, km
0
100
200
300
400
500
600

Figure 9a

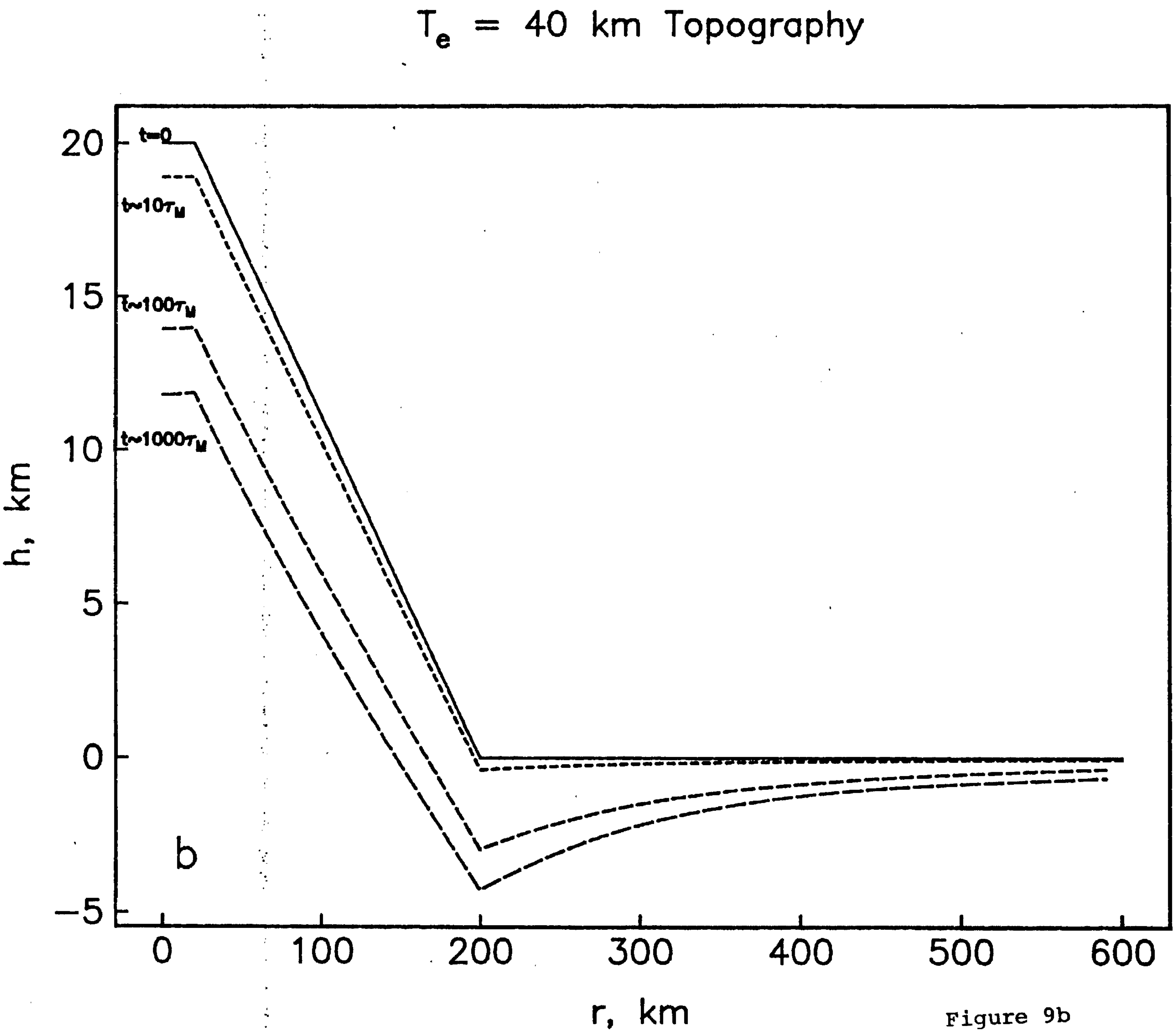

T_e = 40 km Topography
h, km
r, km
20
15
10
5
0
−5
0
100
200
300
400
500
600
t=0
t~10τ_M
t~100τ_M
t~1000τ_M
b

Figure 9b

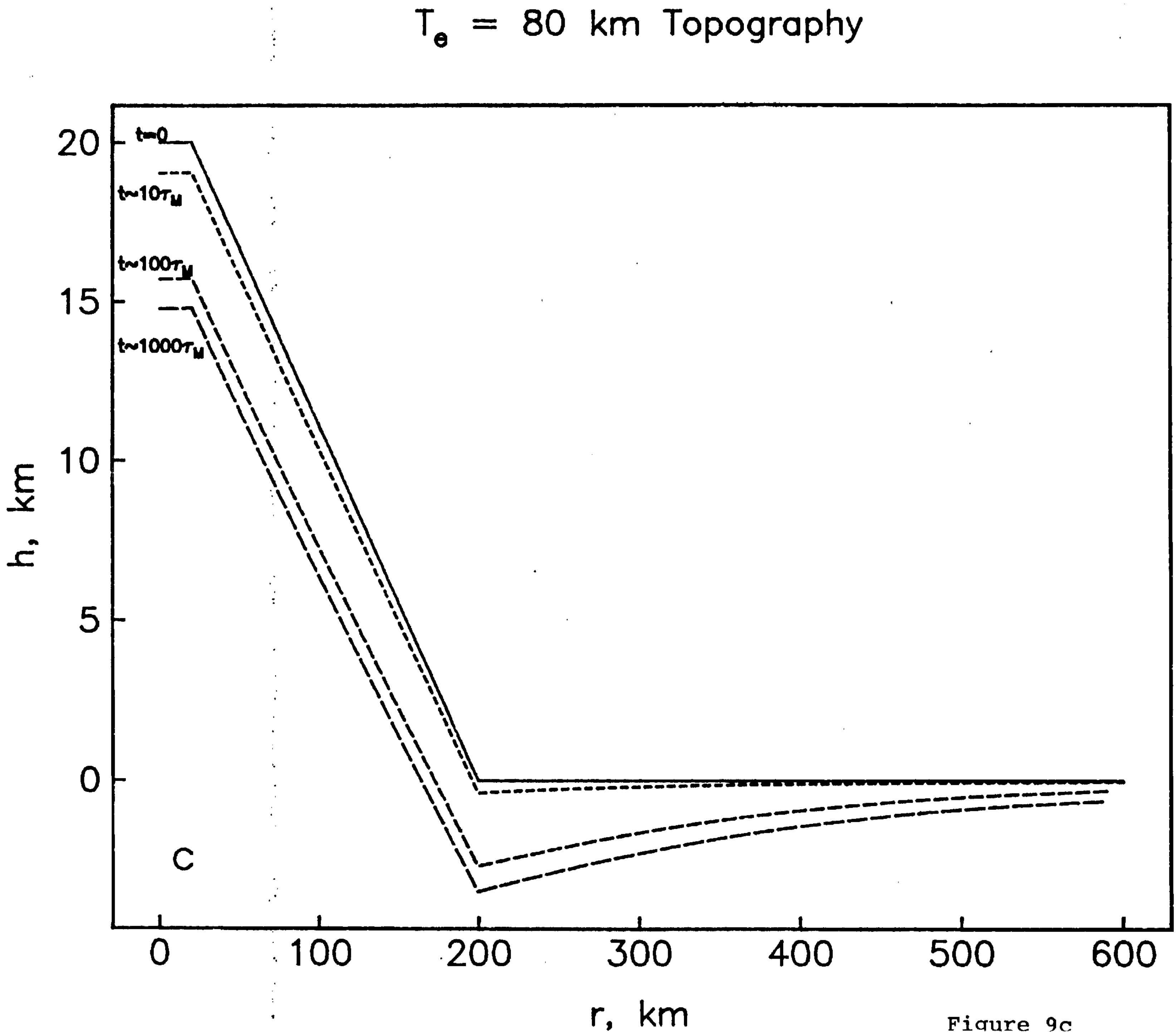

T_e = 80 km Topography
t=0
t~10τ_M
t~100τ_M
t~1000τ_M
C
h, km
20
15
10
5
0
r, km
0
100
200
300
400
500
600

Figure 9c

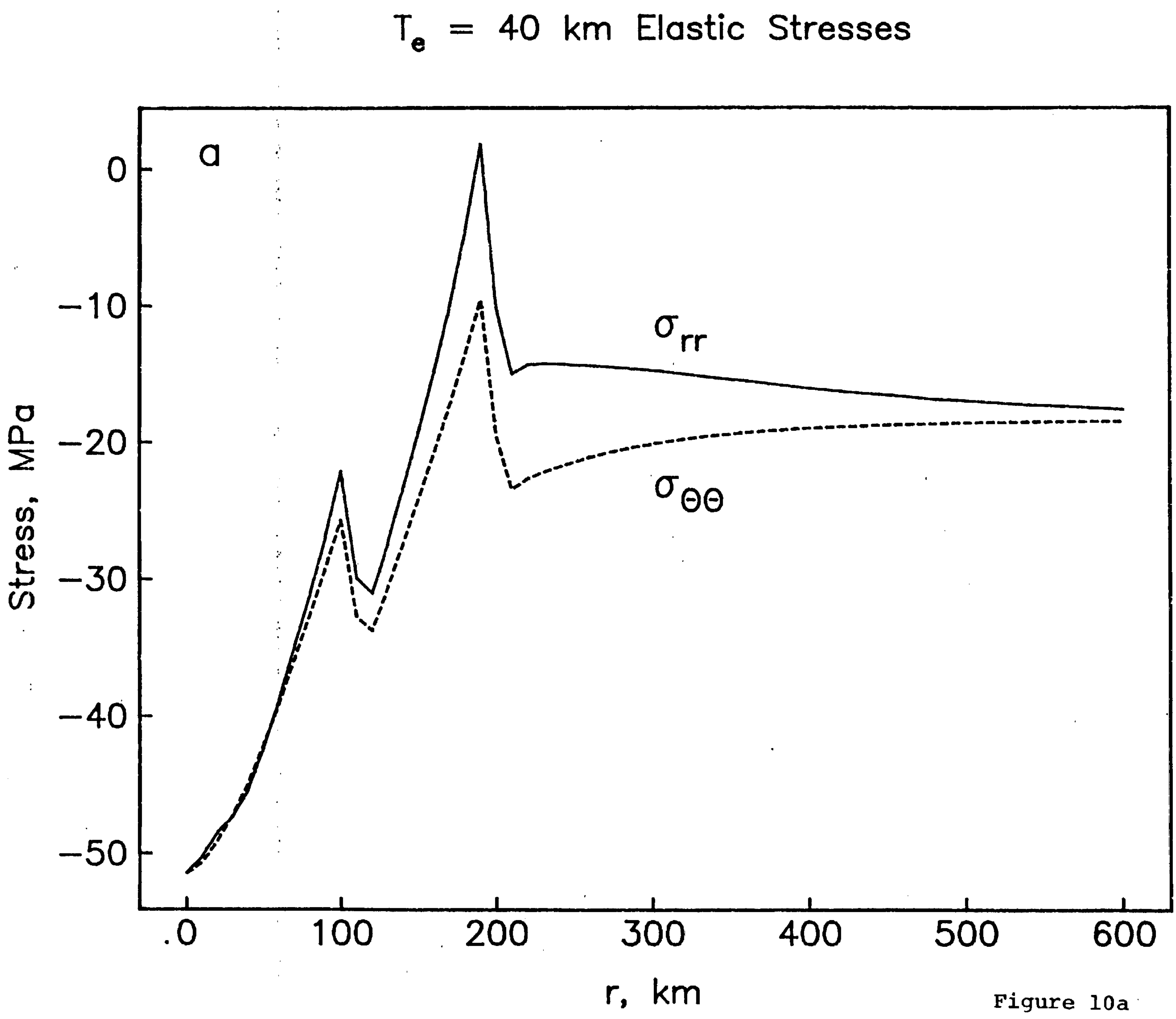

T_e = 40 km Elastic Stresses
a
σ_{rr}
$\sigma_{\Theta\Theta}$
Stress, MPa
0
−10
−20
−30
−40
−50
r, km
.0
100
200
300
400
500
600

Figure 10a

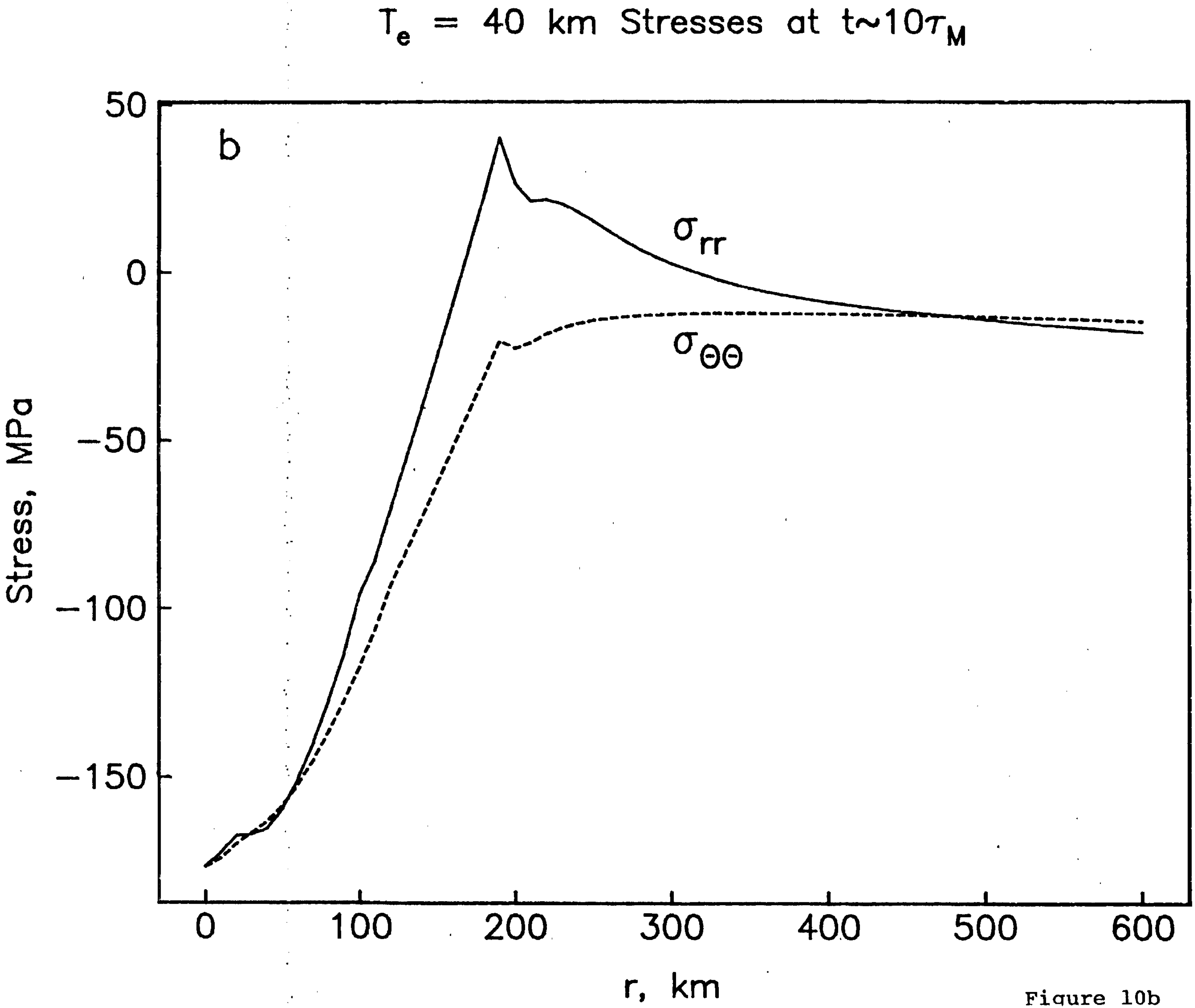
T_e = 40 km Stresses at $t \sim 10\tau_M$
b
σ_{rr}
$\sigma_{\Theta\Theta}$
50
0
−50
−100
−150
Stress, MPa
0
100
200
300
400
500
600
r, km

Figure 10b

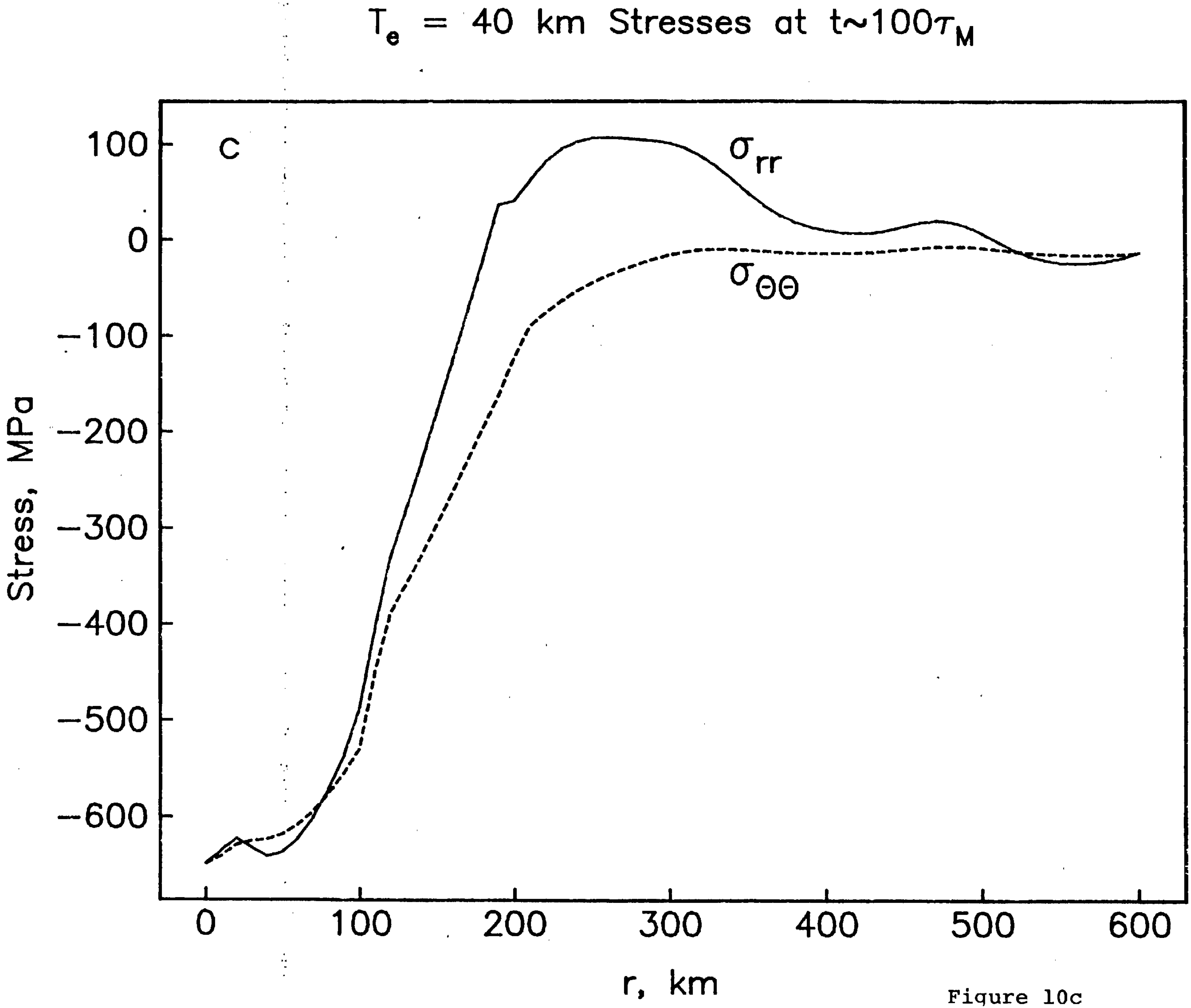

T_e = 40 km Stresses at $t \sim 100\tau_M$

Figure 10c

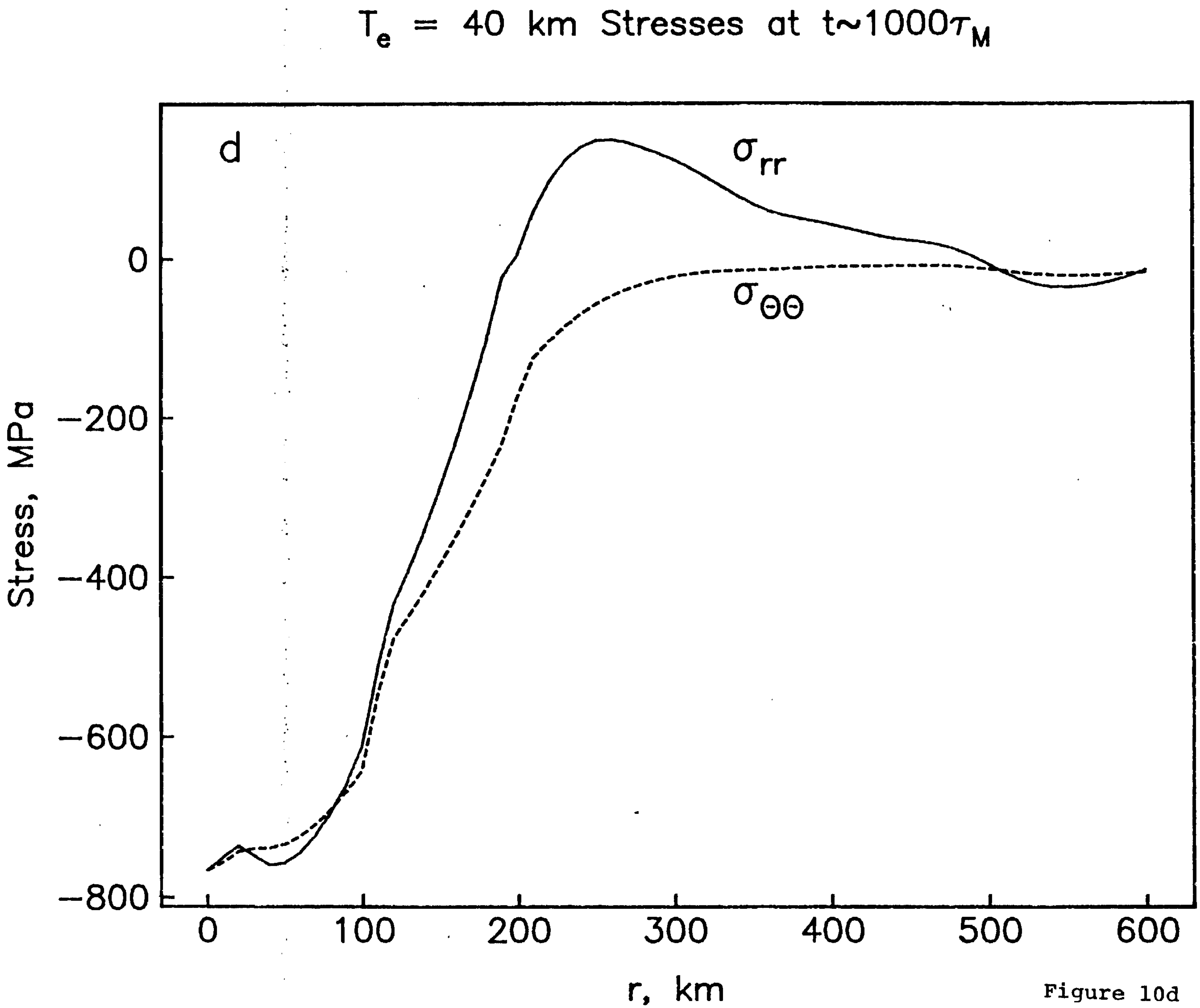
T_e = 40 km Stresses at t~1000τ_M
d
σ_{rr}
$\sigma_{\Theta\Theta}$
Stress, MPa
0
−200
−400
−600
−800
0
100
200
300
400
500
600
r, km

Figure 10d

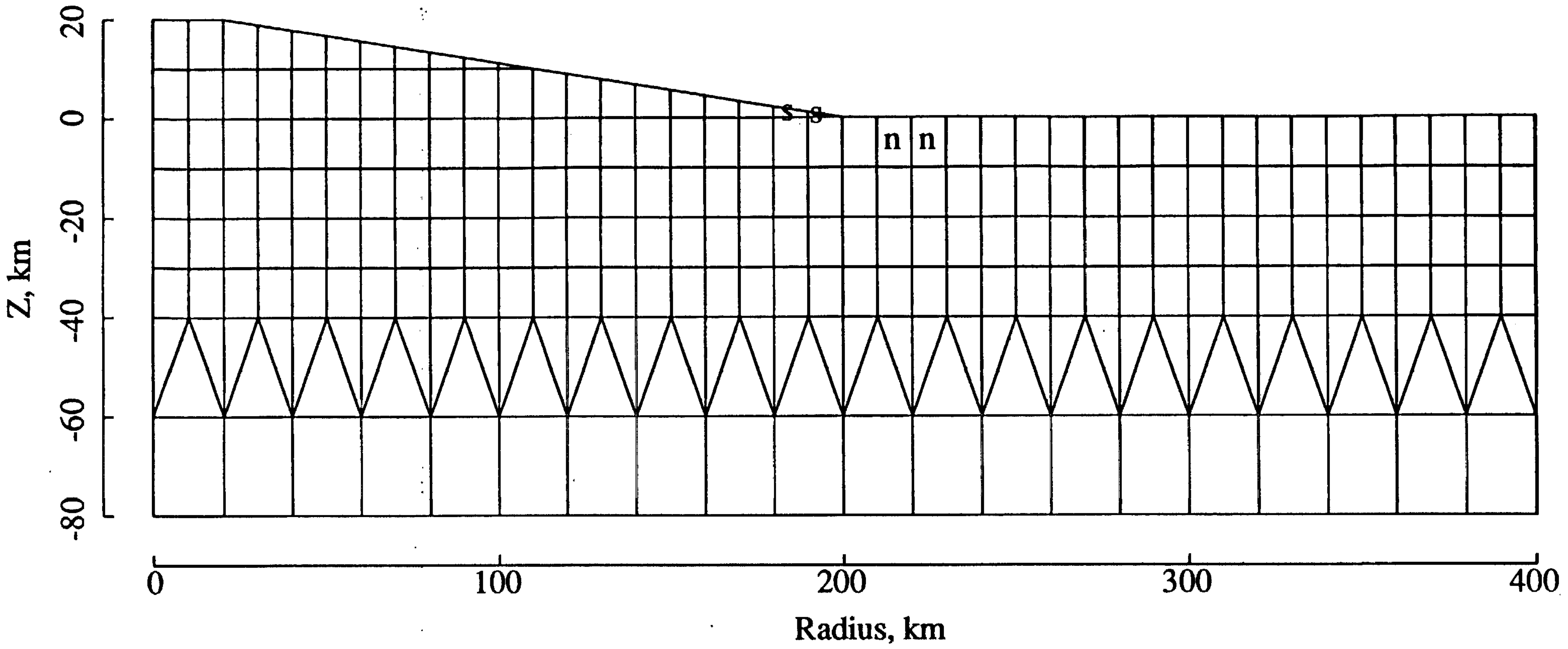

Figure 11a

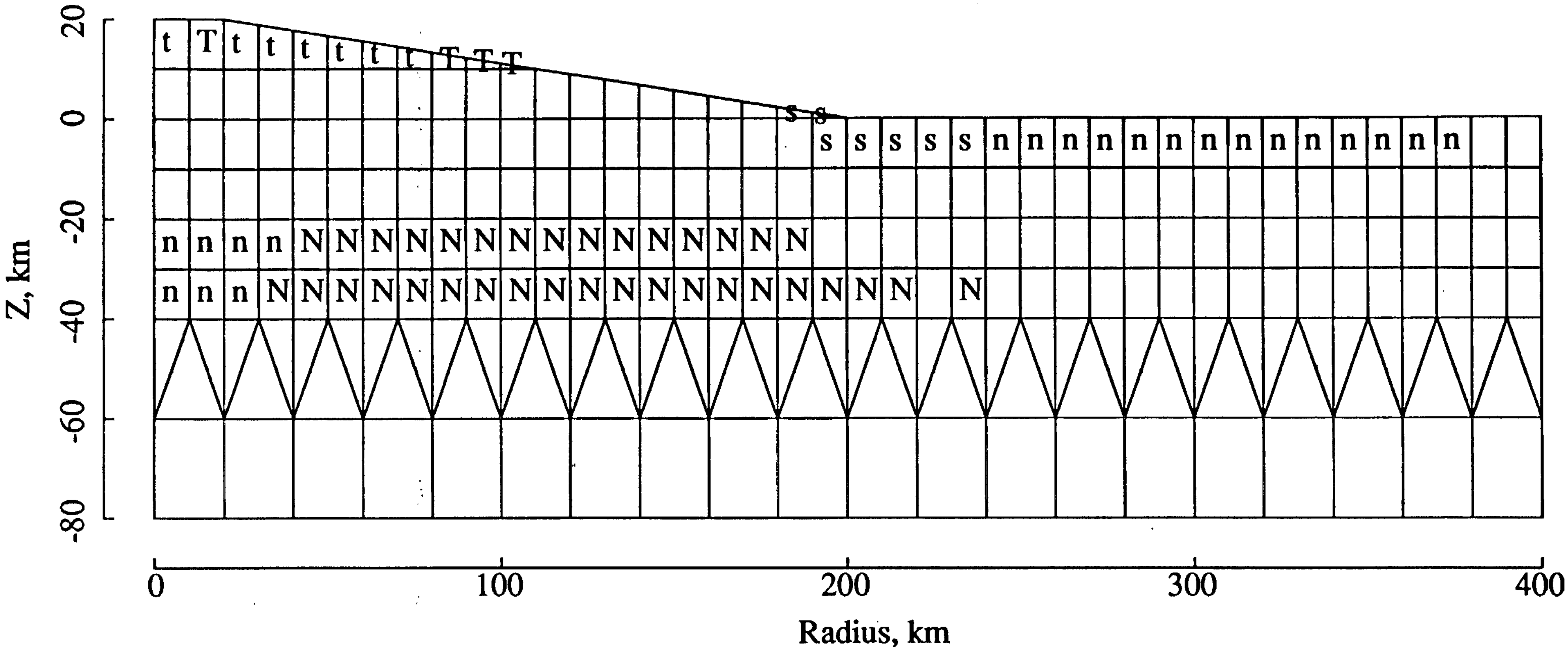
Z, km
20
0
-20
-40
-60
-80
Radius, km
0
100
200
300
400
t T t t t t t t T T T
s s
s s s s s n n n n n n n n n n n n n n
n n n n N N N N N N N N N N N N N N
n n n N N N N N N N N N N N N N N N N N N
N

Figure 11b

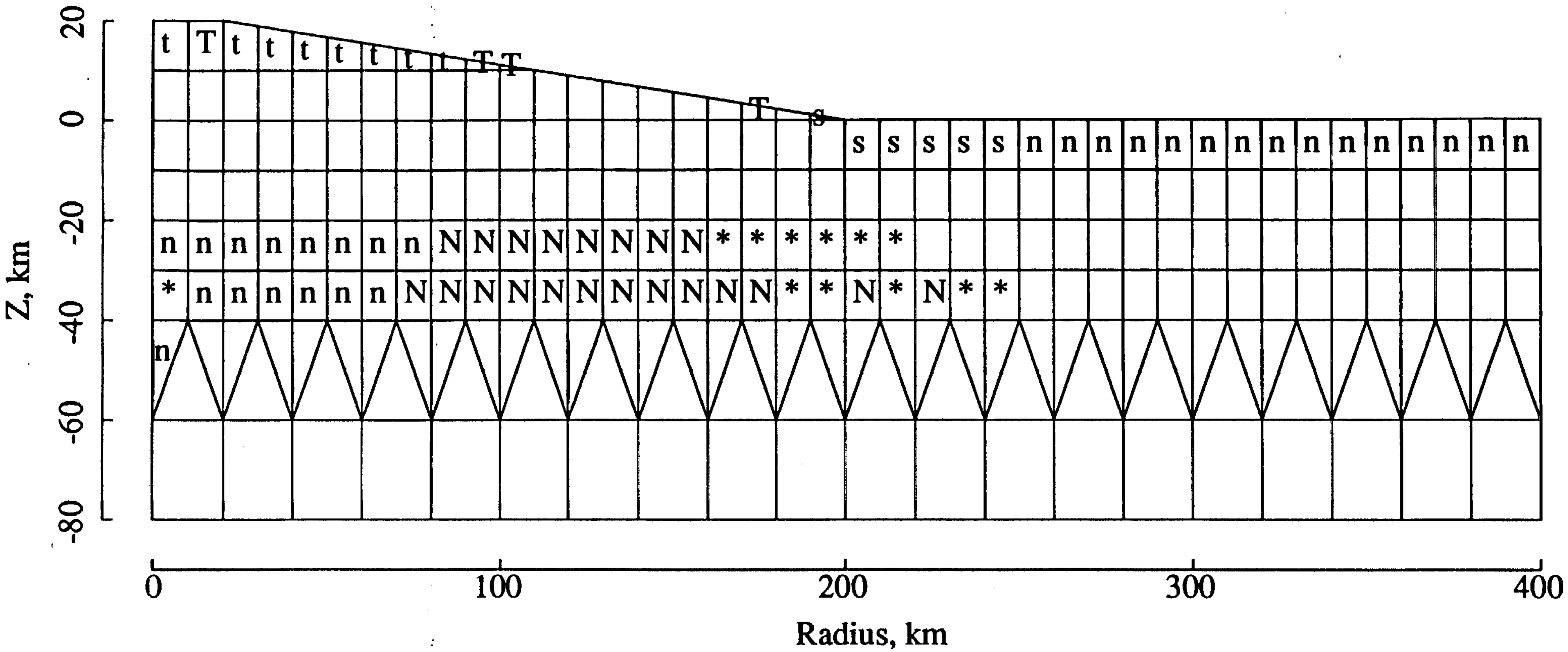
t T t t t t t t t T T
T s
s s s s s n n n n n n n n n n n n n n n
n n n n n n n n N N N N N N N N * * * * * *
* n n n n n n N N N N N N N N N N N * * N * N * *
n
Z, km
20
0
-20
-40
-60
-80
0
100
200
300
400
Radius, km

Figure 11c

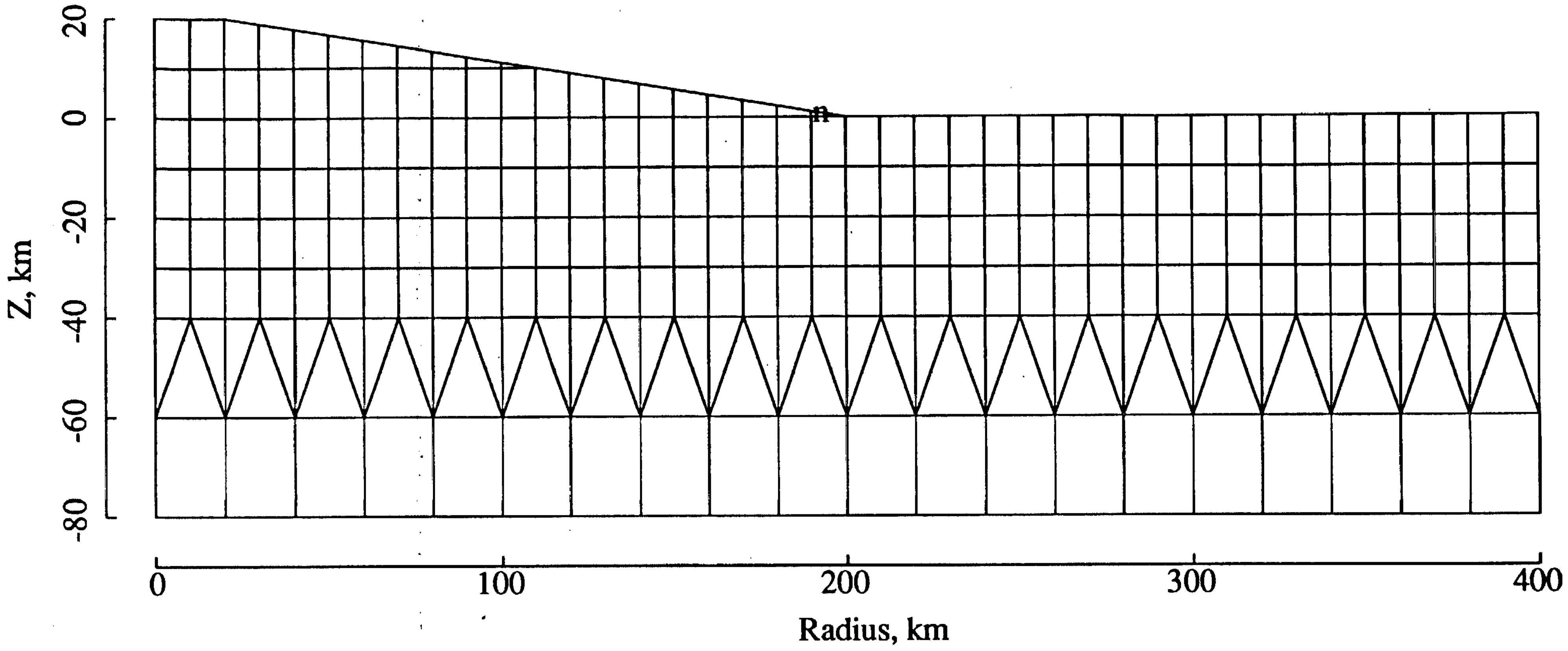

Figure 12a

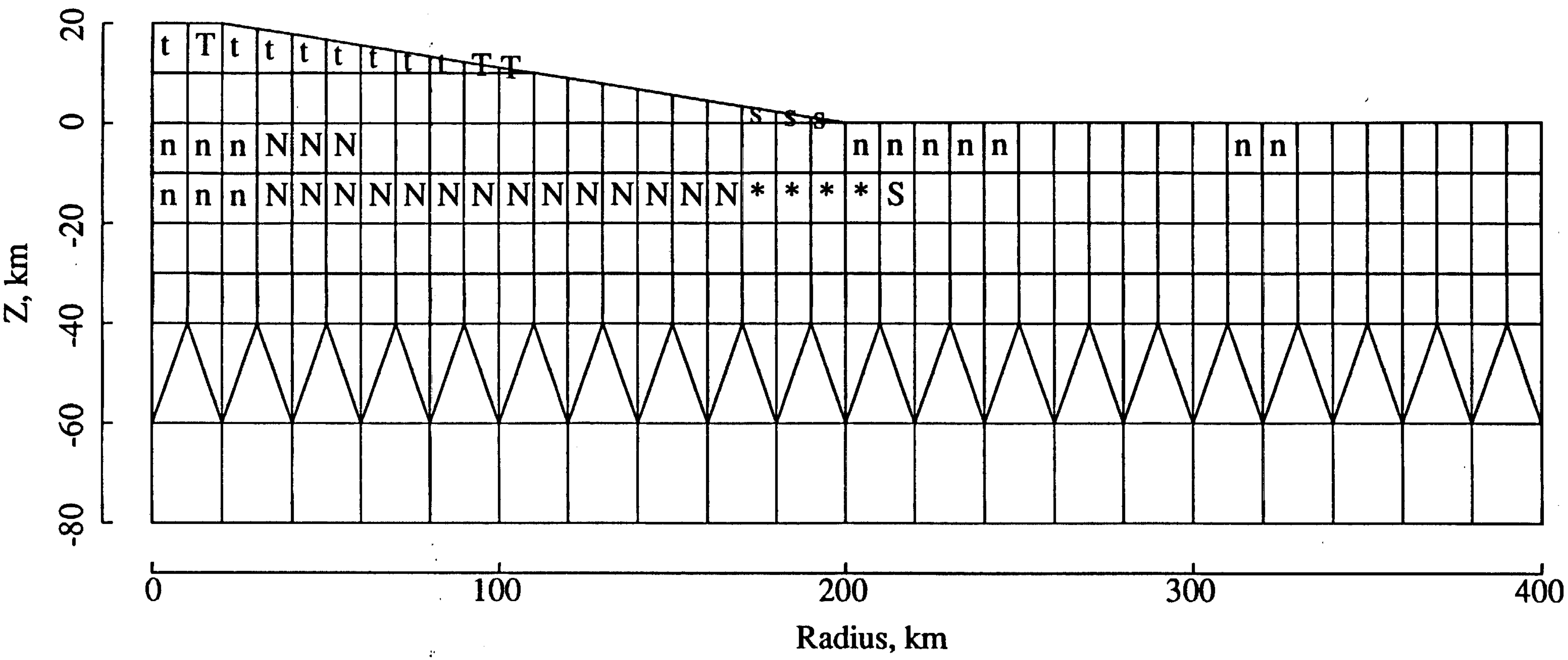
Z, km
20
0
-20
-40
-60
-80
Radius, km
0
100
200
300
400
t T t t t t t t t T T
s s s
n n n N N N n n n n n n n
n n n N N N N N N N N N N N N N N * * * * S

Figure 12b

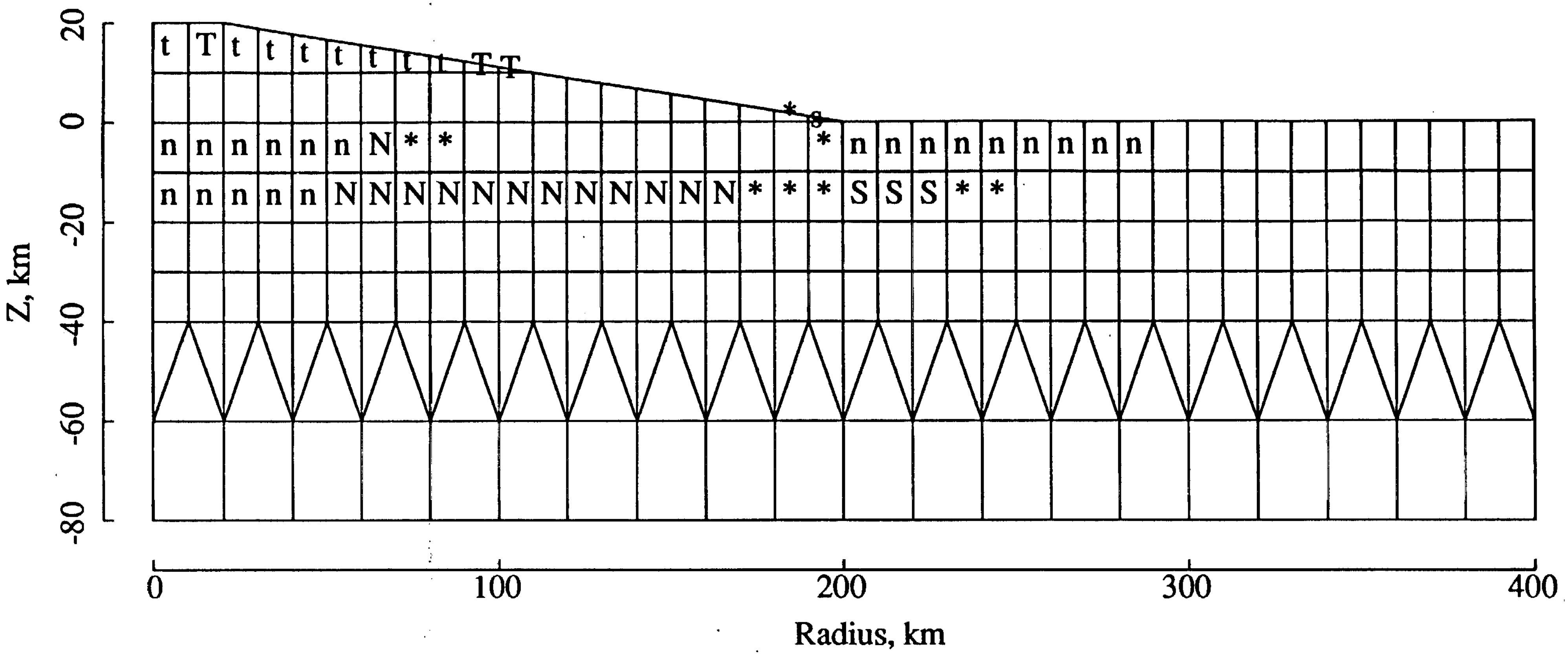
Z, km
20
0
-20
-40
-60
-80
0
100
200
300
400
Radius, km
t T t t t t t t t T T
* s
n n n n n n N * *
*
n n n n n n n n n
n n n n n N N N N N N N N N N N N * * * S S S * *

Figure 12c

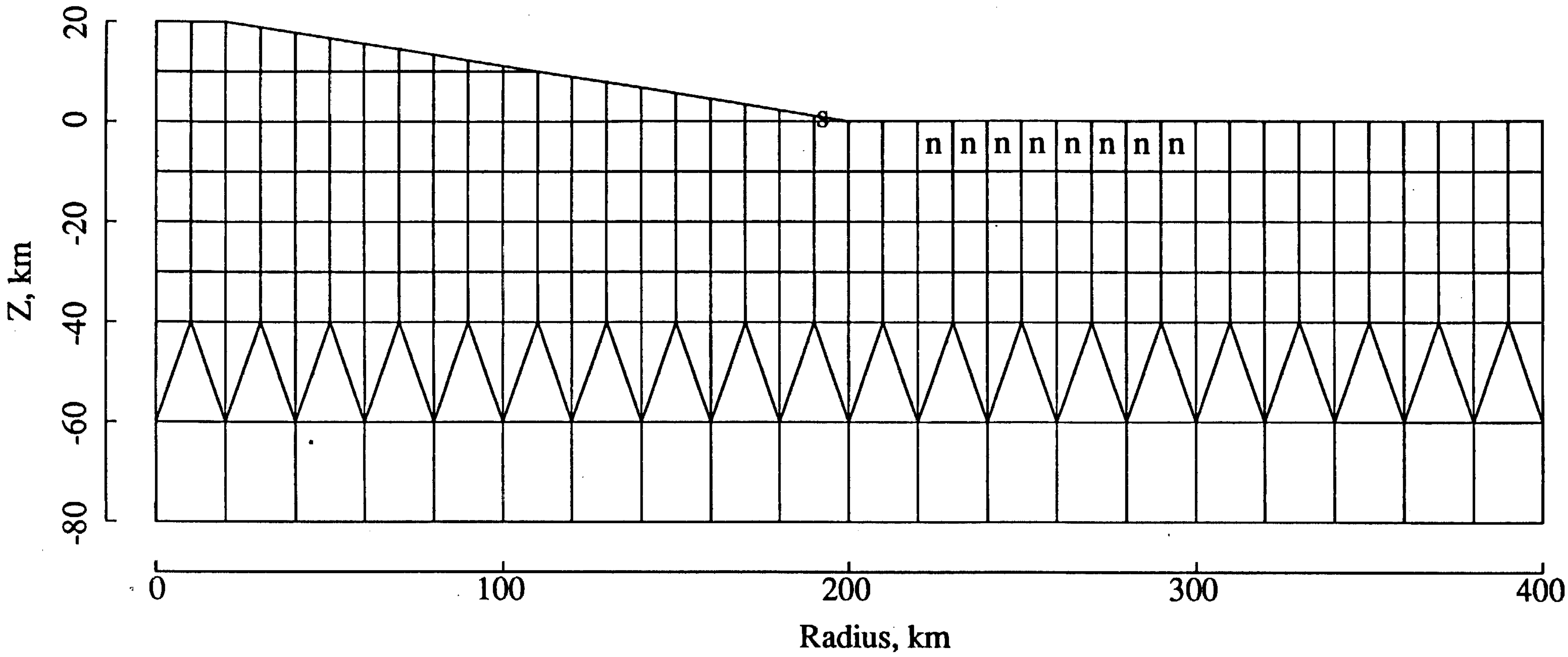

Figure 13a

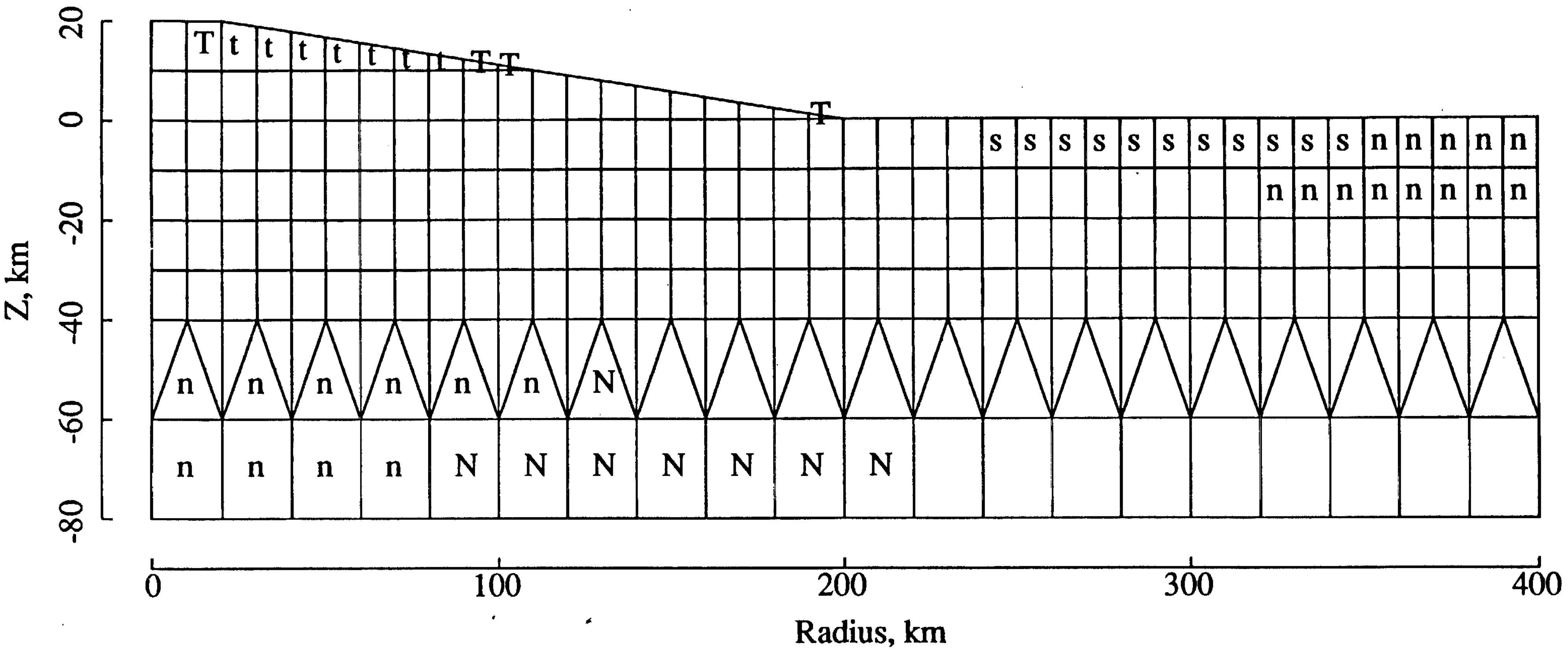
Z, km
20
0
-20
-40
-60
-80
T t t t t t t t T T
T
s s s s s s s s s s s n n n n n
n n n n n n n n
n n n n n n N
n n n n N N N N N N N
0
100
200
300
400
Radius, km

Figure 13c